LIGHTNING PHENOMENOLOGY NOTES

NOTE 4

5 March 1982

A PHYSICAL MODEL OF NUCLEAR LIGHTNING

C. L. Longmire, R. L. Gardner, J. L. Gilbert, and M. H. Frese

Mission Research Corporation

ABSTRACT

In this paper, we present a model consistent with the observed features of nuclear lightning. The problem is divided into two parts. First, an electrostatic problem is solved, modeling the focusing of fields and currents near the tip of the discharge. Second, a detailed self consistent model of the air chemistry, heating rates, and current flow patterns is presented. From the second model the growth rate of the tip is shown to be between 0.8×10^5 m/s and 1.5×10^5 m/s consistent with photographic evidence, and the tip remains sharp, as observed, rather than becoming bulbous and dissipating.

ACKNOWLEDGEMENTS

The authors are grateful to Dr. M. K. Grover who pointed out to us several useful references on the modeling of natural lightning leader channels, Dr. A. V. Phelps who made helpful comments to us during the formative stages of the model and Dr. L. C. Pitchford for discussions about the rate equations used in the model.

CONTENTS

CONTENTS (Concluded)

ILLUSTRATIONS

ILLUSTRATIONS (Concluded)

I. INTRODUCTION

Electrical discharges resembling lightning have been seen on many large-yield surface thermonuclear explosions set off by the United States at Eniwetok and Bikini Atolls in the 1950's. The discharges, observed photographically, and as shown in Figure 1, occur at ranges typically from 900 to 1400 m from the burst and grow along constant radius lines from the ground or ocean surface at a velocity of approximately 10^5 m/s (Ref. 1). The shape of the discharge paths, which are nearly circular with the burst point as the center, strongly suggests that they are driven by the electric field associated with surface burst Electromagnetic Pulse (EMP). Estimates of the EMP environment (Refs. 2 and 3) indicate theta directed electric fields of about 30 kV/m peaking about 1 km from the burst point and at times of a few milliseconds, which is some two orders of magnitude below the uniform field breakdown level of 2.1 MV/m. The photographic evidence is indeterminant as to whether the discharges are associated with vertical structures on the surface.

The physical model for nuclear lightning which we have developed models substantially different physical mechanisms from the processes in natural lightning due to the presence of Compton current and ambient air conductivity. Conductivity of the air is caused by gammas resulting from the capture of neutrons in the ground. The conduction current, which returns the charge deposited in the air by Compton currents to the ground, is focused on the tip of the discharge and heats the air near the tip of the discharge until it becomes a good electrical conductor. The physical model consists of two sets of numerical calculations: The first is the calculation of the collection of conduction current by the tip of the discharge, and the second is the calculation of the heating near the tip (Ref. 3). These calculations are separable because of the large disparity in distance scales between them. The collection of current occurs over a

Figure 1. Lightning strokes observed on IVY MIKE event. Numbers are ground ranges in meters; the lightning channels have been inked for better reproduction.

distance scale of tens of centimeters to tens of meters while the heating occurs over a scale of millimeters. This paper presents a physical mechanism of nuclear lightning which is consistent with the physical observables, i.e., propagation in low fields, velocity of propagation, and observed retention of sharpness of the discharge tip.

The two parts of the model are described in successive sections in the body of the paper. The first section describes a macroscopic model of the focusing of the fields and currents from the EMP environment to a perfectly conducting rod modeling the core and the current flow through the base of the discharge. The next section describes a microscopic self-consistent model of the tip growth. The model is steady state in the discharge tip frame, is centered on the growing tip and covers a region of the order of 1 cm from the tip.

II. PHYSICAL BASIS OF NUCLEAR LIGHTNING

Some time ago, Longmire and Wortman (unpublished) took up the problem defined in the last paragraph of Section 1, i.e., they assumed a conducting channel up to a height h and asked what would happen. They estimated the field intensification at the tip from standard electrostatics formulae, and looked to see if Joule heating near the tip would make the conducting channel grow upward at a rate comparable with the observed rate of about 10^5 m/s. They had two difficulties in getting the model to perform satisfactorily. First, the Joule heating seemed insufficient to yield the observed growth rate. Second, it was not clear that the tip would remain sharp; i.e., it appeared that the tip might grow in all directions, increasing its radius of curvature and decreasing the field and the Joule heating rate.

The turning point came in the present work when we realized that avalanching has a very beneficial effect on the field pattern near the tip. To understand this effect, one first needs to be aware of the ambient state of ionization.

Estimated ambient conductivities are about

$$\sigma = \sigma_e + \sigma_i \approx 4.6 \times 10^{-5} \text{ S/m} \tag{1}$$

and the ambient electric field is

$$E_\theta \approx 3.7 \times 10^4 \text{ V/m} \tag{2}$$

Near the tip of the discharge, the electric field can be very large. If the field E exceeds the avalanche field

$$E_a \approx 2.1 \times 10^6 \text{ V/m} \tag{3}$$

free electrons produce more free electrons faster than they attach. The avalanche rate increases very rapidly with field strength. If E tried to exceed E_a, the electron density would exponentiate in times of the order of 10^{-8} s or less, thus increasing the electron density and the conductivity. As the conductvity increases, the electric field decreases (to carry the same current density) and avalanching stops. Thus avalanching will limit the field to

$$E \leq E_a \tag{4}$$

The limiting happens very rapidly compared with the observed growth rate of the tip; in 10^{-8} s the height increases by only 1 mm. We may therefore assume that wherever E tries to exceed E_a, it will be clamped at the value E_a and the electron density and conductivity adjust to the values needed to pass the required current density.

We visualize the clamping to be a deterministic, smooth process, rather than stochastic or catastrophic. The fact that there are 7.5×10^{14} electrons/m^3 already in the ambient ionization makes this possible. There is a difference here between nuclear lightning and ordinary lightning, where the free electron density is very small initially.

Now consider a thin, perfectly conducting channel extending to a height h above a ground plane, in an ambient electric field E_0 that would be vertical in the absence of the channel. The ambient conductivity is σ_0, and for simplicity we take E_0 and σ_0 to be independent of time and

space. The effect of the conducting channel is to intensify the field near it. There will be an envelope around the channel, of the general shape sketched in Figure 2, inside of which the magnitude of the field E will be clamped at E_a. Outside of the envelope, $E < E_a$ and $\sigma = \sigma_o$. Inside, $\sigma \geq \sigma_o$.

The beneficial effect of avalanching can now be seen. The condition that $E = E_a$ inside the envelope means that the equipotentials there will have constant spacing. Since the channel is an equipotential, the other equipotentials will consist of cylinders about the channel as axis, capped by hemispheres centered about the tip, as indicated in Figure 1. (The envelope is not an equipotential.) It follows that the end cap, the field lines and the current flow are directed precisely into the tip, so that all of the current collected by the end cap flows into the tip. Thus, the result of avalanching is to focus current to the point where it is needed to make the tip grow. We shall estimate the Joule heating from this current-field pattern and show that it can account for the observed growth rate. We shall also estimate the diameter of the tip and explain why it remains sharp. (If it became blunt, Joule heating would fail to maintain the observed growth rate.) Detailed calculations of growth rate will be presented later in this note.

The electrostatics problem associated with determining the envelope can be posed in a variety of ways. We describe one way here; others are described in later sections. In the approximation that the current flow $\vec{J}$ is static, conservation of charge outside the envelope gives

$$0 = \nabla \cdot \vec{J} = \nabla \cdot \sigma_o \vec{E} = \sigma_o \nabla \cdot \vec{E} \quad \text{(exterior)} \qquad (5)$$

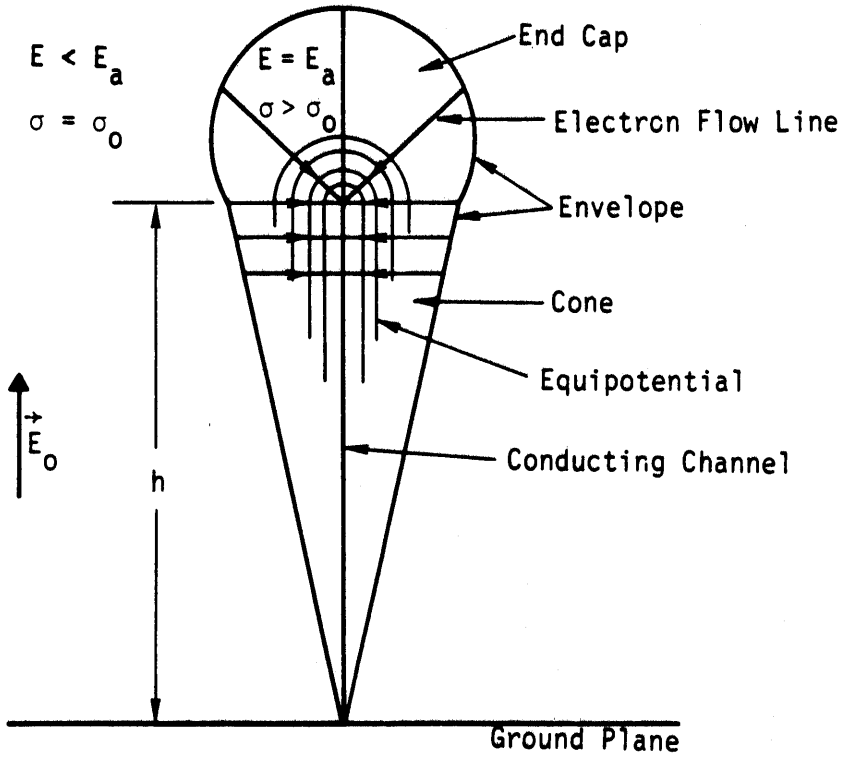

Figure 2. Conducting channel with tip at height h. Envelope is the boundary of the region in which avalanching occurs. The region called the cone is not exactly conical, and the end cap is not exactly spherical.

Thus there is no charge density outside the envelope, except for charges on the ground plane, which terminate the field there. We can eliminate the latter charges from consideration by including the image below the ground plane of the charges inside the envelope. This interior charge density ρ is determined by the model, from the equation

$$\rho = \varepsilon_o \nabla \cdot \vec{E} = \varepsilon_o \frac{1}{r^m} \frac{\partial}{\partial r} r^m E_a$$

$$= \varepsilon_o m \frac{E_a}{r} \quad \text{(interior)} \tag{6}$$

Here r is the spherical or cylindrical radius in the end cap or cone respectively and

$$m = 2 \text{ in end cap,}$$

$$= 1 \text{ in cone.} \tag{7}$$

This charge density extends out to the radius r = R of the envelope. The charge density is finite everywhere, except for the integrable singularity at r = 0; it drops discontinuously to zero at the envelope. The electric field is therefore continuous everywhere, except at r = 0; it is continuous at the envelope.

The potential from this charge density can be written as an integral over the interior of the envelope (including the image). The radius R of the envelope, which is an unknown function of distance z above the ground plane, occurs in the integral. Requiring that the potential from the charge cancel the potential $-E_o z$ of the ambient field at all points along the conducting channel gives an integral equation for R(z). The integral equation can be written as

$$E_o z = \frac{1}{4\pi} \int_{-(h+R)}^{h+\bar{R}} \frac{z'}{|z'|} dz' \int_0^{R_c(z')} \frac{m E_a / r}{\sqrt{r_c^2 + (Z-Z')^2}} 2\pi r_c dr_c \tag{8}$$

Here r_c is the cylindrical radius coordinate measured from the channel axis, R_c is the cylindrical radius corresponding to R, and $\overline{R}$ is the distance from the channel tip at which the envelope cuts the axis (i.e., where $R_c = 0$). It is physically plausible that the equation has solutions. A solution found numerically is presented in following sections. We have some unresolved questions about uniqueness of the solution.

Since the integral equation is homogeneous in powers of the length variables z, z', r and r_c, it is clear that the height h can be scaled out of the probem. It is clear also that the solution depends only on the ratio of E_o to E_a. The solution must be of the form

$$\frac{R_c}{h} = \text{function of } \frac{z}{h} \text{ and } \frac{E_o}{E_a} \tag{9}$$

When R_c or R has been found, the total current collected by the discharge can be calculated immediately. We know that $|\vec{E}| = E_a$ on the envelope and is spherically or cylindrically radial over the end cap or cone respectively. We know that $\sigma = \sigma_o$ on the envelope, from the continuity of $\vec{E}$ and $\vec{J}$. Thus the total current I at the base of the channel is

$$I = \sigma_o E_a \left[\int_0^h 2\pi R dz + \int_{\substack{\text{end} \\ \text{cap}}} R^2 d\Omega \right] \tag{10}$$

Here $d\Omega$ is the element of solid angle about the channel tip.

III. NUCLEAR LIGHTNING ELECTROSTATICS

1. PROBLEM DESCRIPTION

a. Model--Our model is as shown in Figure 3. An electric field $E_0\hat{z}$ is applied to the half space above a perfectly conducting plane at $z = 0$ out of which rises a straight, infinitely thin, perfect conductor of length L. Surrounding it, there are two regions of distinctly different physics; the avalanche or inner region separates the conducting core from the outer region. The entire model is rotationally symmetric with respect to the conductor.

The principal physical assumptions of the model are that

1) All quantities are time independent.

2) The electric field in the inner region points directly away from the nearest point of the conducting core and has a magnitude equal to E_a, the avalanche field strength.

3) The conductivity in the outer region is σ_a, a constant less than the conductivity at any point in the inner region, and the electric field strength in the outer region is not greater than E_a.

In both regions the relevant physical laws are Ohm's Law and Conservation of charge. We seek a steady solution, so the latter is $\nabla \cdot \vec{J} = 0$ in either region and $n \cdot \vec{J}_{outer} = \hat{n} \cdot \vec{J}_{inner}$ on the avalanche boundary.

b. Conditions Along the Avalanche Region Boundary--The tangential components of $\vec{E}$ must be continuous across the avalanche region boundary, otherwise $\nabla \times E$ would have a singularity there and would not be zero, as required of any steady field. This fact along with $|\vec{E}_{outer}| \leq |\vec{E}_{inner}|$ implies that

$$|\vec{n} \cdot \vec{E}_{outer}| \leq |\vec{n} \cdot \vec{E}_{inner}| \qquad (11)$$

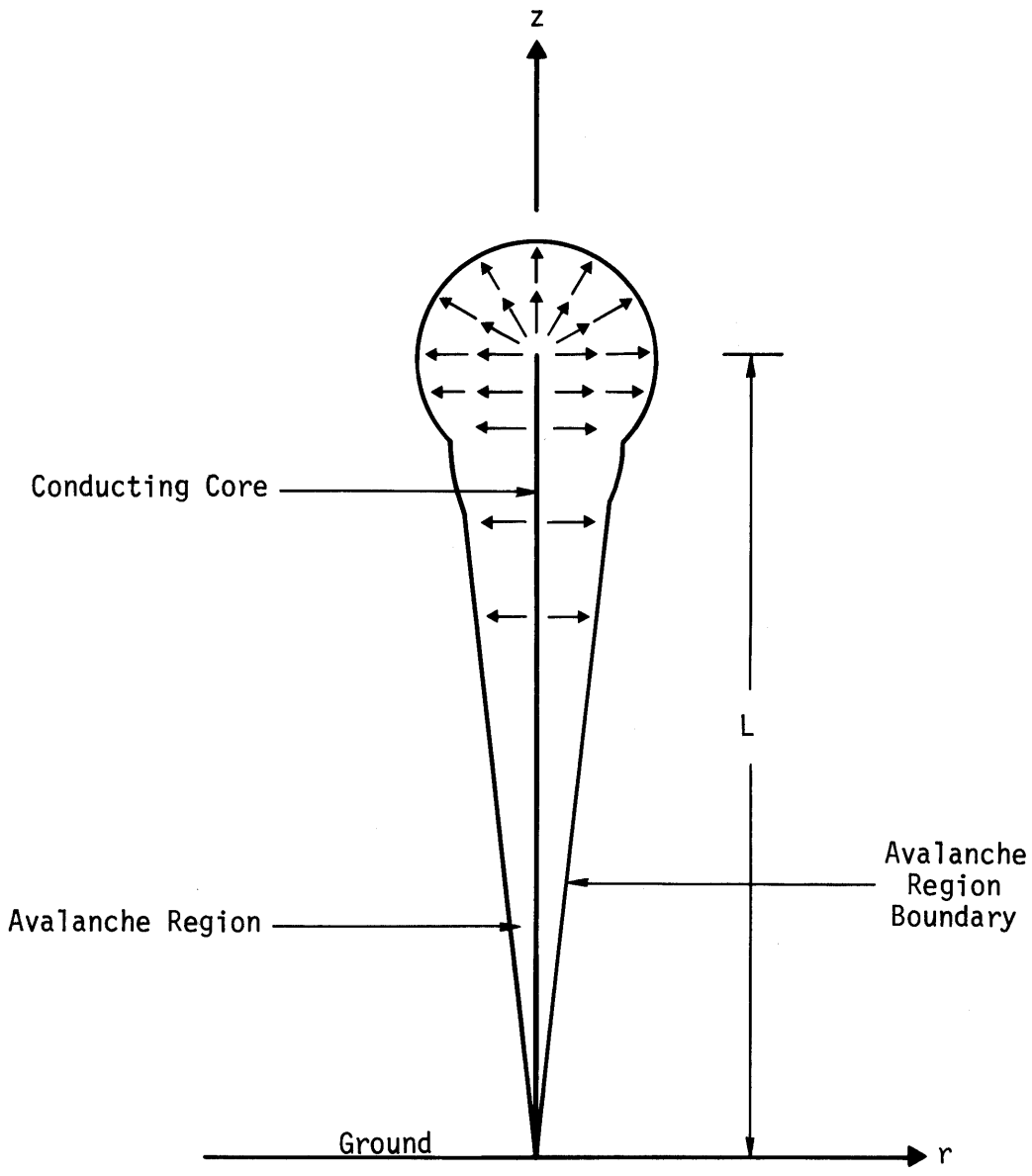

Figure 3. Cross section of cylindrically symmetric lightning stroke model.

along the boundary. Conservation of charge, and Ohm's Law

$$\sigma_{outer}(\vec{n}\cdot\vec{E}_{outer}) = \sigma_{inner}(\vec{n}\cdot\vec{E}_{inner}) \tag{12}$$

and the conductivity assumption $0 \leq \sigma_{outer} \leq \sigma_{inner}$ imply that

$$\left|\vec{n} \cdot \vec{E}_{outer}\right| \geq \left|\vec{n} \cdot \vec{E}_{inner}\right| \tag{13}$$

Thus, from Equations 11 and 13, it follows that the normal component of the electric field must also be continuous across the boundary. Hence, the conditions $\sigma_{outer} \leq \sigma_{inner}$ and $\left|\vec{E}_{outer}\right| \leq \left|\vec{E}_{inner}\right|$ are equivalent to the vector condition

$$\vec{E}_{outer} = \vec{E}_{inner} = E_a\hat{R} \tag{14}$$

where $\hat{R}$ is the unit vector which points away from the nearest point of the conductor.

c. Outer Region Problem--The governing equations in the outer region are $\nabla \times \vec{E} = 0$ and $\nabla \cdot (\sigma_o\vec{E}) = \sigma_o\nabla \cdot \vec{E} = 0$. These may be solved by letting $\vec{E} = -\nabla\phi$ and finding an appropriate solution to $\nabla^2\phi = 0$. The boundary conditions

$$\nabla\phi \to -E_o\hat{z} \text{ as } z^2 + r^2 \to \infty$$

$$\phi = 0 \text{ at } z = 0$$

$$\vec{n} \cdot \nabla\phi = -E_a\vec{n} \cdot \hat{R} \quad \text{on the avalanche region boundary} \tag{15}$$

determine ϕ uniquely for a given boundary. The additional condition that $\vec{t} \cdot \nabla\phi = -E_a\vec{t} \cdot \hat{R}$ for a tangential vector $\vec{t}$, serves to determine the avalanche region boundary.

Alternately, the problem may be stated with a Dirichlet condition (ϕ given) at the avalanche region boundary instead of the Neumann condition ($n \cdot \nabla\phi$ given) above. In the inner region the potential must be $\phi = -E_a R$ where R is the distance to the nearest point on the conductor. Then the problem

$$\nabla^2\phi = 0 \text{ in the outer region}$$

$$\nabla\phi \to -E_0\hat{z} \text{ as } z^2 + r^2 \to \infty$$

$$\phi = 0 \text{ at } z = 0$$

$$\phi = -E_a R \text{ on the avalanche region boundary} \qquad (16)$$

determines ϕ uniquely for a given boundary. And $\vec{t} \cdot \nabla\phi = -E_a\vec{t} \cdot \hat{R}$ on the avalanche boundary is automatically satisfied. The boundary is then determined by imposing $\vec{v} \cdot \nabla\phi = -E_a\vec{v} \cdot \hat{R}$ for any vector $\vec{v}$ not tangent to the boundary. In particular, $\vec{v}$ may be chosen to be $\hat{R}$ so that the additional condition is

$$\hat{R} \cdot \nabla\phi = -E_a \qquad (17)$$

If we nondimensionalize by

$$\phi = LE_a\tilde{\phi}$$

$$(r,z) = L(\tilde{r},\tilde{z}) \qquad (18)$$

these equations become

$$\tilde{\nabla}^2\tilde{\phi} = 0 \text{ in the outer region}$$

$$\tilde{\nabla}\tilde{\phi} \to (E_o/E_a)\tilde{z} \text{ as } \tilde{r}^2 + \tilde{z}^2 \to \infty$$

$$\tilde{\phi} = 0 \text{ at } \tilde{z} = 0$$

$$\left.\begin{aligned} \tilde{\phi} &= -\tilde{R} \\ \tilde{R} \cdot \tilde{\nabla}\phi &= -1 \end{aligned}\right\} \quad \text{on the avalanche region boundary} \tag{19}$$

E_o/E_a is, therefore, the only relevant dimensionless parameter. Note that the length of the conductor has scaled out entirely; it does not appear in this dimensionless parameter.

The problem for the scattered potential

$$\tilde{\nabla}^2\tilde{\psi} = 0 \text{ in outer region}$$

$$\tilde{\psi} \to 0 \text{ as } \tilde{r}^2 + \tilde{z}^2 \to \infty$$

$$\tilde{\psi} = 0 \text{ at } \tilde{z} = 0$$

$$\left.\begin{aligned} \tilde{\psi} &= (E_o/E_a)\tilde{z} - \tilde{R} \\ \hat{R} \cdot (\tilde{\nabla}\tilde{\psi} + \hat{z}) &= -1 \end{aligned}\right\} \quad \text{on the avalanche region boundary} \tag{20}$$

obtained by letting $\tilde{\phi} = \tilde{\psi} - (E_o/E_a)\tilde{z}$ defines the same avalanche region boundary, and is slightly easier to deal with since it has an additional homogeneous boundary condition.

d. Inner Region Problem and Partial Solution--In the inner region, $\vec{E}$ is determined by assumption, and determines σ and $\vec{J}$ once the boundary shape is known. These will be of critical importance for estimates of the growth rate of this structure.

For the coordinate system shown in Figure 4 we have

$$J_\theta = 0 \text{ above } z = L$$

$$J_z = 0 \text{ below } z = L \tag{21}$$

and $J_\phi = 0$ everywhere. Therefore,

$$\nabla \cdot J = \frac{1}{R^m} \frac{\partial}{\partial R} \left(R^m J_R \right) = 0 \tag{22}$$

where

$$m = \begin{cases} 2 & z > L \\ 1 & z < L \end{cases} \tag{23}$$

So

$$R^m J_R = \begin{cases} c_1(z) & m = 1 \\ c_2(\theta) & m = 2 \end{cases} \tag{24}$$

or

$$J_R = \frac{c_m}{R^m} \tag{25}$$

If the avalanche region boundary is $R = R_a$ then c_m may be determined from $J_R\big|_{R_a} = \sigma_o E_a = c_m / R_a^m$ where σ_o is the outer region conductivity. Thus,

$$J_R = \sigma_o E_a \left(\frac{R_a}{R} \right)^m \tag{26}$$

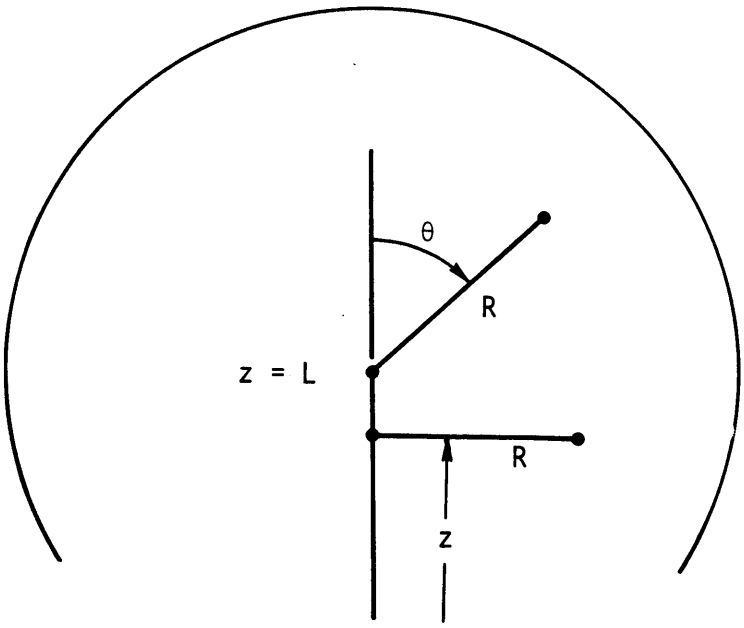

Figure 4. Inner region coordinate system.

and, of course,

$$\sigma = \sigma_o \left(\frac{R_a}{R}\right)^m \tag{27}$$

This last equation implies a discontinuity in σ at $z = L$ for $R < R_a$ (since m changes from 1 to 2 there). This would not have to be if the conductor were not assumed to be infinitesimal in size.

The total current in the conductor is equal to the total current through the avalanche boundary

$$I = \int \vec{J} \cdot \vec{n} d\sigma \tag{28}$$

Where S is the avalanche region boundary and $\hat{n}$ is the unit normal vector. If $\hat{n} \sim \hat{R}$, as will be seen to be true, then since $\vec{J} = \sigma_o E_a \hat{R}$ along the boundary this current is

$$I = \int_S \vec{J} \cdot \hat{R} d\sigma = \sigma_o E_a \int_S d\sigma = \sigma_o E_a A(S) \tag{29}$$

Where A is the area of the surface.

2. METHOD OF SOLUTION FOR OUTER REGION PROBLEM

We solve the outer region problem for the avalanche boundary by an iteration scheme involving the following steps:

1) Guess the boundary

2) Solve the potential problem expressed in the first 4 relations of Equation 20

3) Use the resulting $\vec{E} = \nabla\psi$ to move the boundary toward satisfaction of $\hat{R} \cdot (\nabla\tilde{\psi} + \hat{z}) = -1$

4) Test the degree of convergence and either stop or go back to 2 above.

In this section some of the details of these steps are discussed.

a. Potential Problem Solver--The basic approach used to solve the potential problem of Equation 20 is to find a linear combination of analytic solutions to

$$\tilde{\nabla}^2\tilde{\psi} = 0$$

$$\tilde{\psi} \to 0 \text{ as } \tilde{r}^2 + \tilde{z}^2 \to \infty$$

$$\tilde{\psi} = 0 \text{ at } \tilde{z} = 0 \qquad (30)$$

which as nearly as possible satisfies

$$\tilde{\psi} = (E_o/E_a)\tilde{z} - \tilde{R} \text{ on the avalanche boundary} \qquad (31)$$

The analytic solutions used are the potentials due to charge distributed along the z-axis with a triangular distribution as shown in Figure 5 (for these potentials, see Appendix A). Any sum of these potentials is a potential due to a continuous piecewise-linear charge distribution. And since the triangular bases overlap, the potential due to any continuous piecewise-linear charge distribution with discontinuities in derivative only at end points of the specified segmentation can be written as a sum of them. In addition, the potential due to a pair of point charges of opposite sign, one at the top of the charge carrying segment and the other oppositely located with respect to z = 0 is included. Since all these solutions are dipole distributions, they satisfy Equation 30. Because all conditions of Equation 30 are homogeneous, any sum of these potentials must also satisfy them. This is the reason for solving the scattered problem.

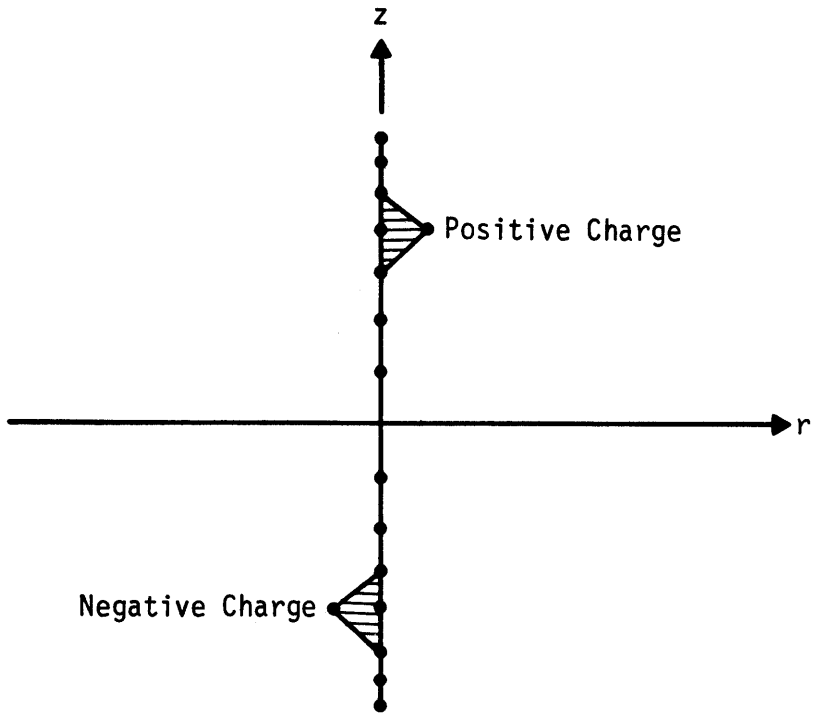

Figure 5. Charge distribution for analytic potential and field.

The method of collocation is used to derive a system of equations for the coefficients of the linear combination. That is, a set of points $\{(r_j,z_j)\,|\,j = 1,\ldots,m\}$ is chosen to represent the boundary, and then Equation 31 is applied to the linear combination at each of these points. If the potentials are $\{\phi_i\,|\,i = 1,\ldots,n\}$, then the system

$$\sum_{i=1}^{n} c_i\phi_i(r_j,z_j) = (E_o/E_a)z_j - R(r_j,z_j) \qquad j = 1, \ldots, m \tag{32}$$

results for the unknowns $\{c_i\,|\,i = 1,\ldots,n\}$.

Finally, these equations are solved in a least square error sense. In the results to be presented later, the number of equations (m, the number of observation points) is approximately two and one-half times the number of unknowns (n, the number of potentials). Some error in satisfying the inhomogeneous boundary condition results; but the reduced error at intermediate points on the boundary due to the superiority in numerical stability of least square solution ($n < m$) over exact solution ($n = m$) more than compensates.

This method of solving the potential problem expressed in Equations 30 and 31 has several advantages. The most relevant of these is that since the ϕ_i are analytically known, so are the fields $\vec{E}_i = -\nabla\phi_i$. Thus, the field $\underset{\sim}{\vec{E}} = -\nabla\tilde{\psi}$ can be computed from the c_i by

$$\tilde{E} = -\nabla\tilde{\psi} = -\sum_{i=1}^{n} c_i\nabla\phi_i \tag{33}$$

No numerical differencing need be done. This offers a substantial increase in accuracy over grid methods. The fields $-\nabla\phi_i$ are given in Appendix A. Straightforward evaluation leads to loss of precision due to cancellation, so a scheme for accurate evaluation is also discussed there.

b. Boundary Mover--After the potential problem is solved for two initial boundaries, each boundary point (r_j,z_j) is moved radially (i.e., along $\hat{R}$) an amount which would make $[\hat{R} \cdot (\nabla\psi + \hat{z}) + 1](r_j,z_j) = 0$ if this quantity were a linear function of (r_j,z_j) and did not depend on (r_k,z_k) for $k \neq j$ (secant method). The change in radial distance $R(r_j,z_j)$ is limited to a doubling or halving of the current distance. The bottom point $(r_1,0)$ needs separate treatment since $\hat{R} \cdot (\nabla\psi + \hat{z}) = 0$ there, but the position of this point has weak influence on the rest of the problem and no physical interest. It is forced to lie on the cone projected from the two points above it or to have half the radius of the point above it, whichever is greater.

This relatively simple procedure works remarkably well. After only eight iterations, the maximum relative change in position of the top 90 percent (well outside the influence of the bottom point) is less than 10^{-4} on the run for $E_o/E_a = 0.001$ reported below.

c. Initial Boundaries--The two initial boundaries are both cones topped with ellipsoids. The first tapers from a radius of 0.01 m at the $z = 0$ to approximately $E_oL/4E_a$ at $z = L$. The half ellipsoid joins the cone at $z = L$ forming an ice-cream-cone-like structure. The semimajor axis is vertical and 1.5 times the semiminor axis. The second initial boundary is the first expanded by 10 percent in the $\hat{R}$ direction.

d. Discretization--The charge distribution extends approximately $1/3(E_oL/4E_a)$ above the end of the conductor. The spacing of both boundary points and charge segment endpoints is smaller at the top, with the latter being about 4 times the former at $z = L$. The results, to be presented below, were generated using 201 boundary points with 25 on the head (above $z = L$) and 80 charge segments.

e. Implementation--The algorithm described above was implemented in a highly vectdorized Fortran computer code requiring approximately a half second of CRAY-1 CPU time per iteration.

3. RESULTS

Since the length of the conductor scales completely out of the problem, we are free to arbitrarily fix it. The problems here all were solved with L = 300 m, a representative length for a nuclear device lightning stroke at 30 ms after the detonation.

The avalanche boundary is shown for E_o/E_a = 0.001, 0.002, 0.005, 0.01, 0.02, and 0.05 in Figures 6, 7 and 8. In each of those figures (a) shows the boundary below the top of the conductor with the axial scale compressed greatly relative to the radial scale, and (b) shows the boundary near the top of the conductor with equal axial and radial scales. The radial scale on (a) and both scales on (b) change from figure to figure; the size of the avalanche region increases with increasing E_o/E_a. Note that, except in the region just below the head, $\hat{n}$ is well approximated by $\hat{R}$; so Equation 32 gives a quite satisfactory approximation for the current.

The numerical results are given in Table 1. The current given here is determined from Equation 29 using $\sigma_o = 2.6 \times 10^{-5}$ mho/m and $E_a = 2.1 \times 10^6$ V/m. Thus, the current shown is 96 A/m^2 times the area. The field error shown is the maximum difference of the magnitude of the field $E = -\nabla\tilde{\psi} - \hat{z}$ from 1 at any point (r_j, z_j) along the boundary, excepting the bottom point. It is the maximum relative error in satisfying the field boundary condition. The potential error is the square error in solving Equation 35 divided by the sum of the squares of the right-hand side of that same equation, which is a measure of the relative error in satisfying the potential boundary condition. There is <u>no</u> error in satisfying Equation 33 since our solution is a sum of exact solutions to these equations.

Longmire (unpublished) has shown that the area of the avalanche region boundary should be approximated by an expression of the form

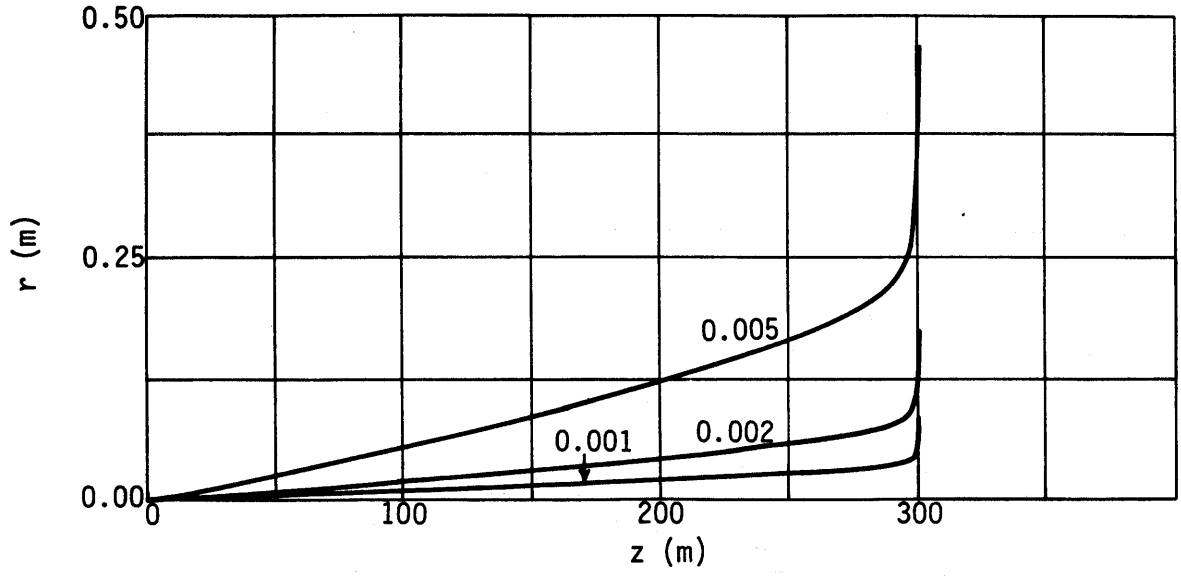

a. Body

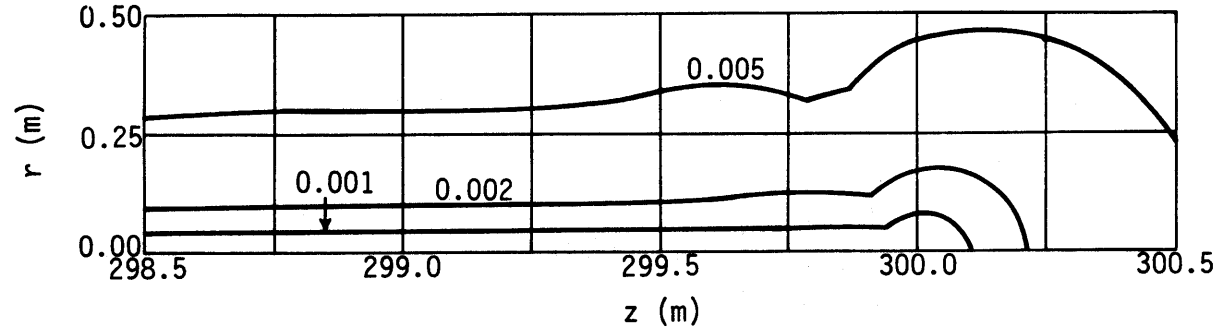

b. Head

Figure 6. Avalanche region boundary for E_o/E_a = 0.001, 0.002, 0.005.

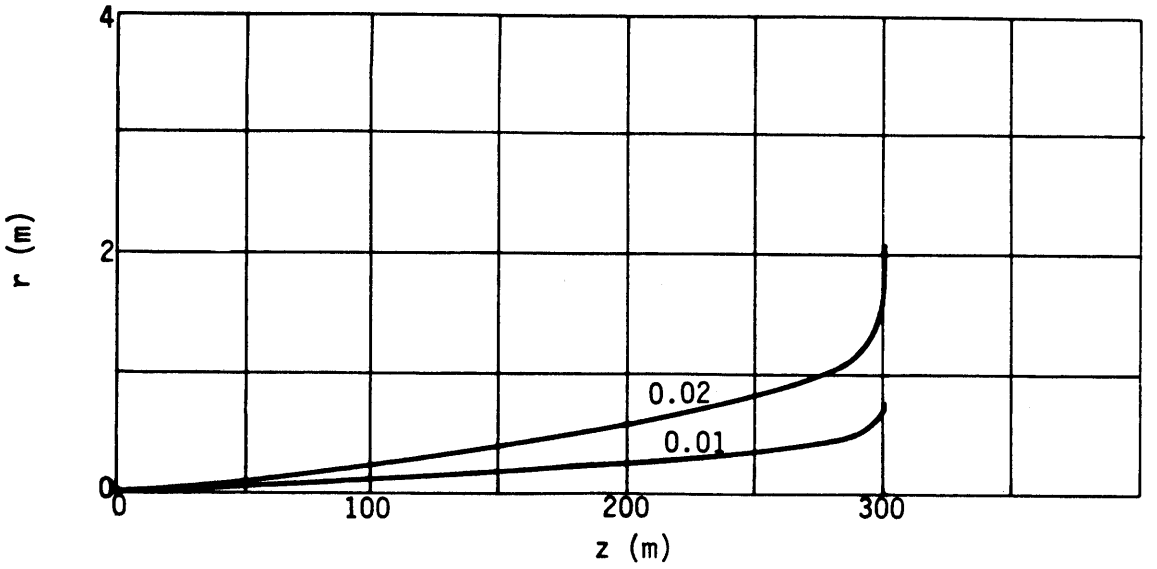

a. Body

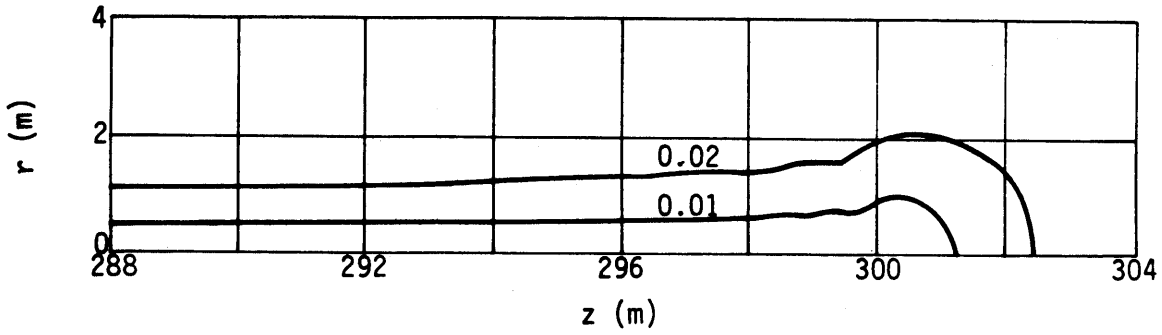

b. Head

Figure 7. Avalanche region boundary for E_o/E_a = 0.01, 0.02.

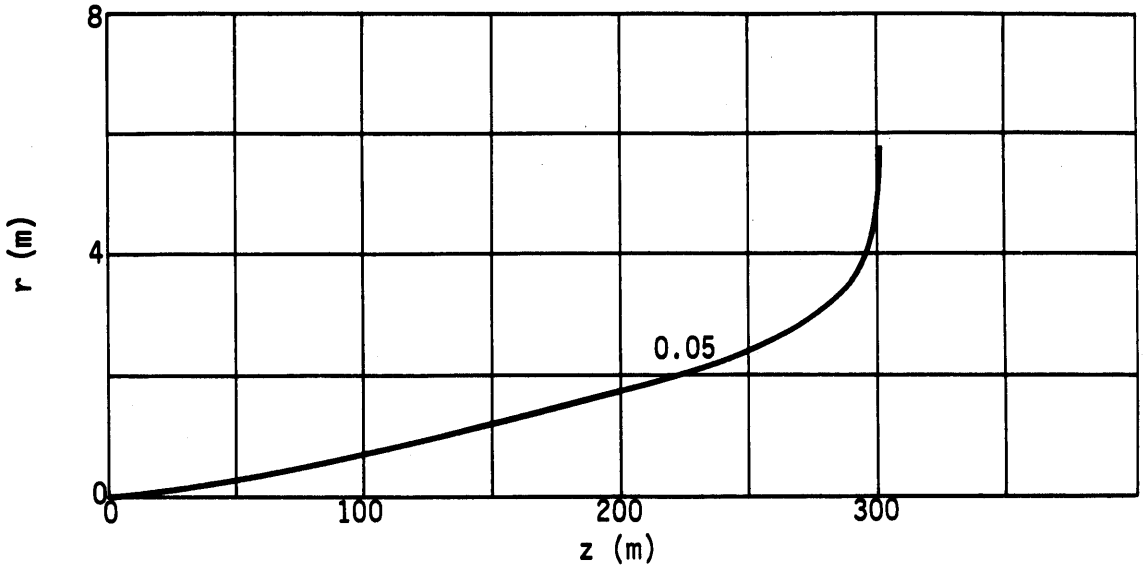

a. Body

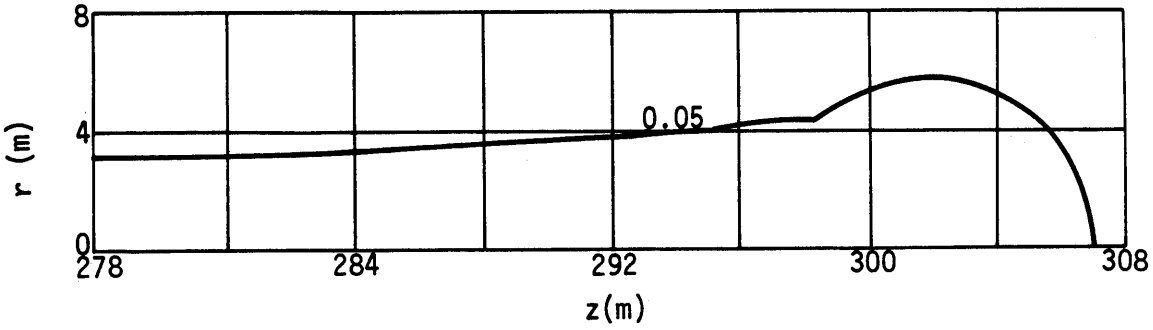

b. Head

Figure 8. Avalanche region boundary for E_o/E_a = 0.05.

TABLE 1. NUMERICAL RESULTS

E_o/E_a	Area (m^2)	Current (A)	Radius of Head (m)	Field Error (%)	Potential Error (%)
0.001	28.9	2,800	0.0830	2.0	0.17
0.002	62.8	6,100	0.174	2.0	0.14
0.005	178.0	17,000	0.464	0.7	0.09
0.010	398.0	38,000	0.979	0.2	0.05
0.020	907.0	88,000	2.08	0.1	0.05
0.050	2820.0	272,000	5.72	0.1	0.05

$$\text{Area} = \frac{\pi L^2 E_o/E_a}{C_1 - C_2 \ln(E_o/E_a)} \tag{34}$$

Figure 9 shows the values of $(E_o/E_a)/\text{Area}$ versus E_o/E_a from Table 1 as dark circles on a semilog plot. Also shown is a linear fit to those results which gives

$$\text{Area} \simeq \frac{\pi L^2 E_o/E_a}{1.644 - 1.178 \ln(E_o/E_a)} \tag{35}$$

This fits the results within one-half of one percent for E_o/E_a from 0.001 to 0.02. Figure 10 shows a similar plot of $(E_o/E_a)/(\text{Radius of Head})$ from which

$$\text{Radius of Head} = \frac{L(E_o/E_a)}{1.973 - 0.238 \ln(E_o/E_a)} \tag{36}$$

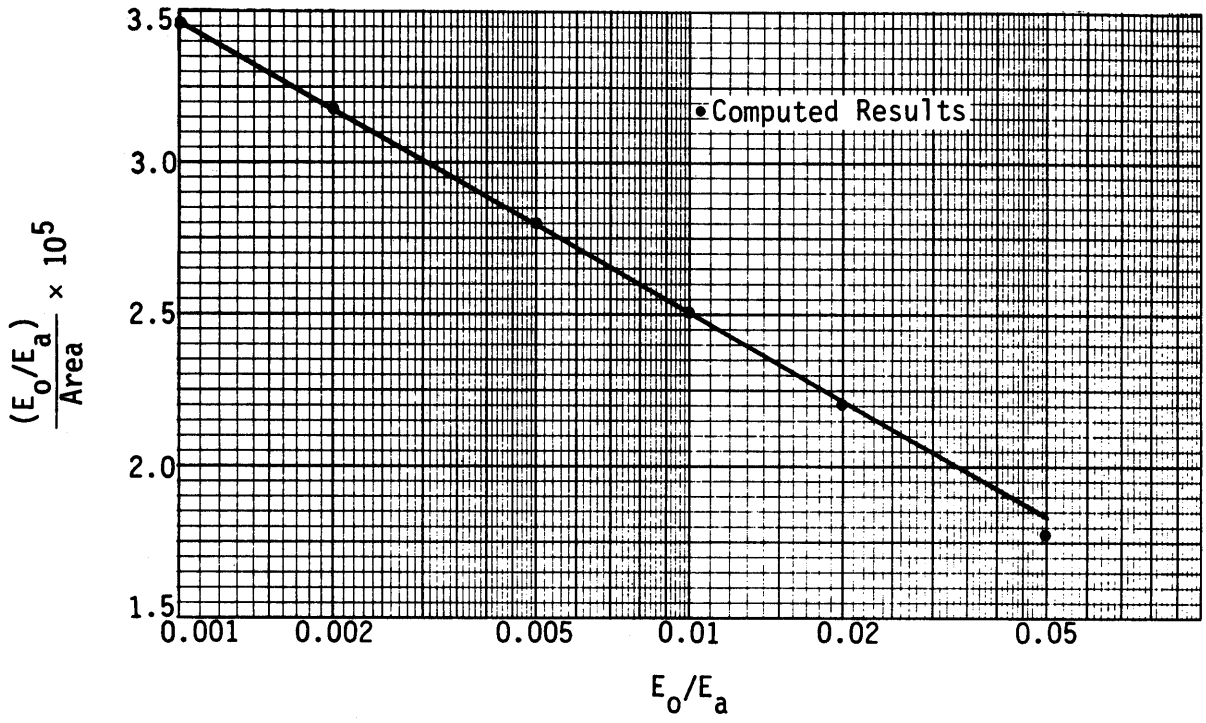

Figure 9. Comparison of fit to computed results for area.

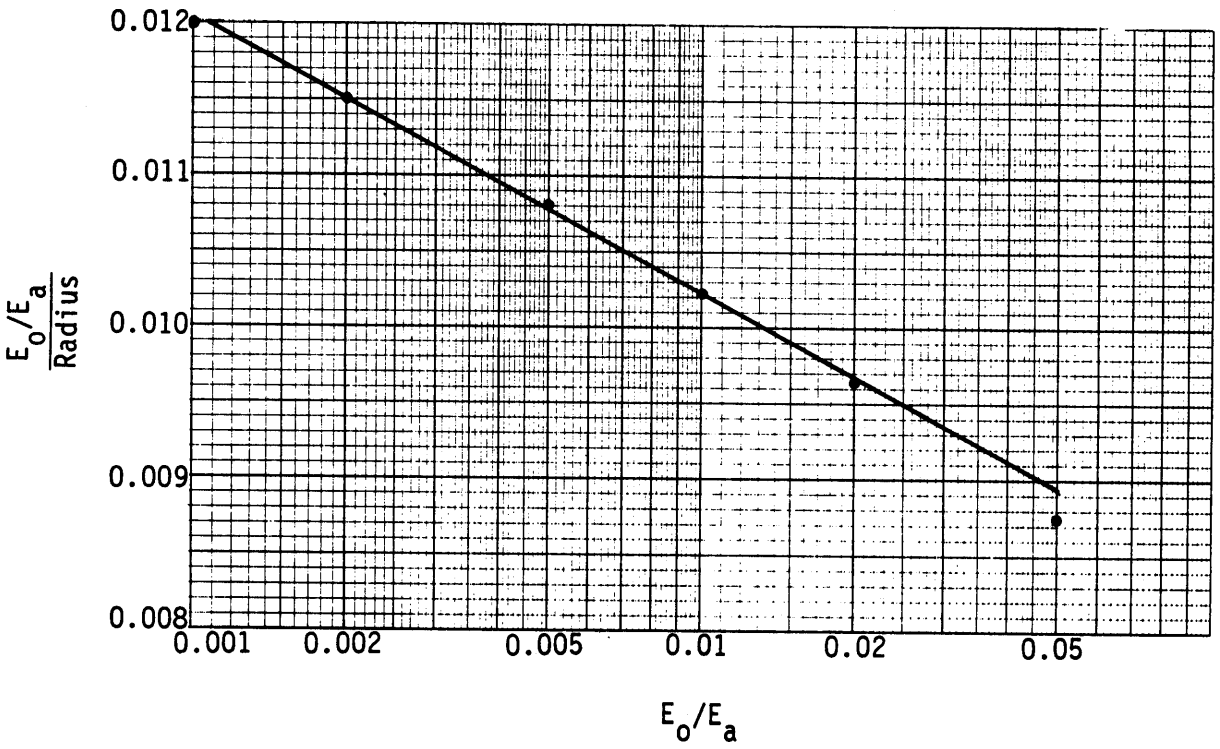

Figure 10. Comparison of fit to computed results for radius.

IV. GROWTH OF THE DISCHARGE

We shall now discuss in a qualitative way the mechanisms of growth of the conducting channel. Quantitative calculation of the growth rate is presented in the remaining sections of this report.

Our supposition is that the tip of the conducting channel grows upward by Joule heating of the air just above the tip to a temperature of the order of 1 eV, at which point it becomes thermally ionized, so that a large electric field is no longer needed to maintain a high electron density and conductivity. We shall examine the Joule heating rate below in a typical case.

We also need to explain why the tip remains sharp as it grows upward, rather than become bulbous (which would reduce the Joule heating rate). The reason is the parallel path Joule heating instability; if two (or more) resistors in parallel are driven by a fixed total current, and if the resistance decreases with increasing temperature, then one resistor will become very hot and carry all the current. It is reasonably evident that this instability will make the growing tip (and the channel) as small in diameter as possible, with the smallness limited only by heat conduction.

Let us now examine the Joule heating rate, assuming that the electric field is $E_a = 2.1 \times 10^6$ V/m. Taking the ambient field $E_o = 3.7 \times 10^4$ V/m and assuming the channel height h = 334 m, we find from Equation 36 the radius of the envelope head,

$$R \approx 2 \text{ m} \tag{37}$$

The current density at spherical radius r from the tip is therefore

$$J = \sigma_o E_a \frac{R^2}{r^2} \approx \frac{400}{r^2} \text{ A/m}^2 \tag{38}$$

and the Joule heating rate is

$$P = JE_a \approx \frac{10^9}{r^2} \quad W/m^3 \tag{39}$$

The energy required to heat air to a temperature of 11600 K (1 eV) is

$$Q = 4 \times 10^7 \quad J/m^3 \quad \text{at normal density} \tag{40}$$

If the radius of the tip is a and the growth rate is v (m/s), then we must have

$$Pa^3 \approx Qa^2v$$

or

$$Pa \approx Qv \tag{41}$$

From Equations 39 and 40, this becomes

$$\frac{10^9}{a} \approx 4 \times 10^7 v \tag{42}$$

Taking the observed $v \approx 10^5$ m/s gives

$$a \approx \frac{10^9}{4 \times 10^{12}} = 2.5 \times 10^4 \text{ m} \tag{43}$$

This may seem like a very small radius. However, it is substantially larger than the minimum radius allowed by heat conduction. The mean free path of a molecule in air is

$$\lambda \approx 3 \times 10^{-7} \text{ m} \tag{44}$$

and the thermal speed at a temperature of 11600 K (1 eV) is

$$u = 3 \times 10^{3} \text{ m/s} \tag{45}$$

Note that the observed growth speed v is much larger than the thermal speed u,

$$\frac{v}{u} \approx 30 \tag{46}$$

This means that the growth is supersonic, and neither molecular diffusion nor hydrodynamics can play a strong role in the growth of the tip. We presume that either electronic or radiative heat conduction limits the smallness of the tip.

It appears that our model can account for the observed growth rate of the discharges. The theory of the tip follows in subsequent sections.

Finally, we note that if a is known, Equation 42 determines the growth speed,

$$v \approx \frac{Pa}{Q} = \frac{JE_a a}{Q} = \frac{\sigma_o E_a^2 R^2}{Qa} \tag{47}$$

R depends on E_o and h through Equation 36.

V. THE REGION NEAR THE TIP

After developing a suitable basis for the macroscopic behavior of nuclear lightning we can concentrate on the region within several centimeters of the tip. At a radius of about 2 cm, the electron density becomes high enough that dissociative electron-ion recombination becomes more important than attachment and the electric field rises until a balance is obtained between avalanche and recombination. As we approach the tip, the Joule heating of the air by the conduction current causes dissocation of the positive ions so that the dissociative recombination can no longer occur and the electron density increases rapidly, combined with a decrease in the electric field. At this point, the air within a few tenths of a millimeter of the center line of the discharge has been heated to well above 11600 K (1 eV) and thermal ionization is sufficient to keep the electron density high even though the electric field becomes small.

The two-dimensional variation in the conductivity near the tip requires us to simultaneously solve the air chemistry equations, thermal rate equations and the electric field, which is determined by the steady state continuity equation

$$\vec{\nabla} \cdot \vec{J} = \vec{\nabla} \cdot \sigma\vec{E} = 0 \tag{48}$$

In order to use a finite difference grid with very small cells where the Joule heating of the air is important and conserve computer resources by using large finite difference cells elsewhere, the equations are transformed into a frame moving upward so that the "tip" of the discharge remains stationary in the moving frame. Convective derivatives resulting from this transformation are very important in the thermal rate equations. Hydrodynamic effects are unimportant near the tip because the tip growth rate is much larger than the thermal speed of the molecules.

The air density is calculated from a three species model with electrons and positive and negative ions, with rate coefficients corrected for dissociation. Physical processes included in the air chemistry model include:

1. Avalanche, (collisional ionization),
2. Dissociative (two body) attachment,
3. Ion-ion and electron-ion recombination,
4. Thermal detachment and detachment by collisions with free electrons.

Physical processes in the thermal model include:

1. Joule (ohmic) heating
2. Separate calculation of molecular vibrational energy density and energy transfer to the thermal pool,
3. Radiative cooling.

These processes are used with a reduced (molecular vibrational energy removed), complex (internal energy and pressure contributions of ionization and dissociation included) equation of state to determine the gas temperature.

The flow of conduction current is calculated by solving the continuity equation on a prolate spheroidal mesh with the air chemistry and thermal equations (which determine the conductivity variation in space and time). The boundary conditions on the current are determined by the electric field and total current in the avalanche region, as prescribed in the previous sections. The calculational mesh is centered on the moving tip and the equations are allowed to evolve in time until equilibrium conditions are reached. There is only a narrow range of tip propagation velocities centered around 1.2×10^5 m/s for which a steady state solution is approached.

The next section deals with a one-dimensional code which was written to gain an understanding of the air chemistry processes and examine numerical methods for solving these equations which involve rate coefficients differing by many orders of magnitude. In this code, the conduction current is prescribed to have a $1/r^2$ convergence towards the tip so that no solution of the steady state continuity equation is required.

Section VII contains a description of the extension of the code to two-dimensions in prolate spheroidal coordinates. The two-dimensional air-chemistry code is also integrated with a two-dimensional solver of the current continuity equation so that the currents and electric fields are determined self-consistently. Finally, in the last section, the results of the studies of the tip growth are discussed.

VI. ONE DIMENSIONAL CODE

To provide a test bed for various air chemistry options and numerical methods a one-dimensional code modeling a narrow cone above the tip of the discharge was developed. Spherical geometry and a fixed converging current density of $400/r^2$ A/m^2 were used. The air chemistry and thermal equations were allowed to develop and determine the conductivity, electric field and heating rates. Chosen reactions of the air chemistry are described below.

1. CURRENT

A fixed, radially convergent, current was used in the one-dimensional code so that it would not be necessary to solve the continuity equations simultaneously with the air chemistry and thermal rate equations. This limits the applicability of the one-dimensional solution to radii beyond about 3×10^{-4} m. Inside this radius, the air is thermally ionized and the current flow becomes primarily vertical rather than radial.

Estimated electronic and ionic conductivities are

$$\sigma_e \sim 3.2 \times 10^{-5} \text{ S/m}$$

$$\sigma_i \sim 1.4 \times 10^{-5} \text{ S/m}$$

$$\sigma_{tot} \sim 4.6 \times 10^{-5} \text{ S/m} \qquad (49)$$

The vertical electric field can be estimated assuming $E_\theta \gg E_r$. From Reference 2

$$E_\theta \sim 3.7 \times 10^{4} \text{ V/m} \qquad (50)$$

With an avalanche electric field of

$$E_a = 2.1 \times 10^6 \text{ V/m} \tag{51}$$

the radius of the avalanche region around the tip can be obtained from Equation 36. For a height of 334 m, the avalanche region radius is 2 m and the total current in the avalanche region is

$$I = 2\pi r^2 \sigma E_a$$

$$= 2400 \text{ A} \tag{52}$$

and the current density is $400/r^2$ A/m^2 with r in meters

2. AIR CHEMISTRY

The choices available for the particular set of reactions used in the description of the air chemistry are far ranging. Examples of previous calculations range from two species and one reaction to over 100 species and 500 reactions. As discussed in the introduction to this section, a one-dimensional code with a spherically converging current density of $400/r^2$ A/m^2 was written to investigate the electronic and chemical reactions. The various reactions were followed through the rate equations to develop the appropriate species populations for a steady state solution, for a gaiven velocity of tip growth. The reactions used are described below along with methods used for calculating them. While the rate constants show some time dependence at early times (Refs. 4 and 5), this variation was ignored for simplicity and becuase the time scales are somewhat shorter than those considered here. Populations of three charged species, (i.e., electrons, negative ions and positive ions) were tracked. This choice is consistent with the work of E. Marode's group (Ref. 6), and that of Gallimberti (Ref. 7) who have studied various discharge mechanisms. The

choice does not allow complete consideration of the effects of dissociation or variations in ionization energies or cross sections between different molecular species in air.

These three species are allowed to interact through the following processes. These results represent best values found for the particular reactions.

a. Attachment

Formation of negative ions at high electric fields is primarily due to the process of dissociative attachment. For the three body attachment rate (Ref. 8):

$$\alpha_3(s^{-1}) = 10^8 \frac{0.62 + 800\ E_o^2}{1 + 10^3 E_o^2 [E_o(1+0.03E_o^2)]^{1/3}} \tag{53}$$

and for the two body (dissociative) rate

$$\alpha_2(s^{-1}) = 1.22 \times 10^8\ e^{-42.3/E_o} \tag{54}$$

where $E_o = 3.34 \times 10^{-5}$ E, where E is the electric field in dry air at atmospheric pressure in V/m. Dry air is assumed throughout. Finally, the total attachment rate is

$$\alpha = \alpha_2 + \alpha_3 \tag{55}$$

Since the mechanism at the high electric fields near the tip is primarily dissociative, the attachment rate is reduced by the fraction of ions which have been thermally dissociated.

b. Avalanche (Reference 8)

Electrons accelerated in large electric fields generate additional electrons by collisions with neutral species. The rate used for that mechanism is

$$G(s^{-1}) = \frac{5.7 \times 10^{8}\ Y^{5}}{1 + 0.3\ Y^{2.5}} \tag{56}$$

where $Y = 3.34 \times 10^{-7}\ E$. The rates for the curve fits for avalanche and attachment were compared to recent experimental values reported by Phelps.* The agreement is quite good as noted by the comparison in Figure 11.

c. Electron-Ion Recombination (Reference 6)

Assumed to have a constant rate

$$a_{ei} = 10^{-13}\ m^{3}/s \tag{57}$$

d. Ion-Ion Recombination (Reference 6)

This mechanism is assumed to be reduced by the gas temperature to 5/2 power.

$$a_{ii} = 2.6 \times 10^{-6}(T_o/T_g)^{2.5} \tag{58}$$

where $T_o = 300$ K.

---

*Phelps, A. V., Private communication to C. L. Longmire, 1 December 1980.

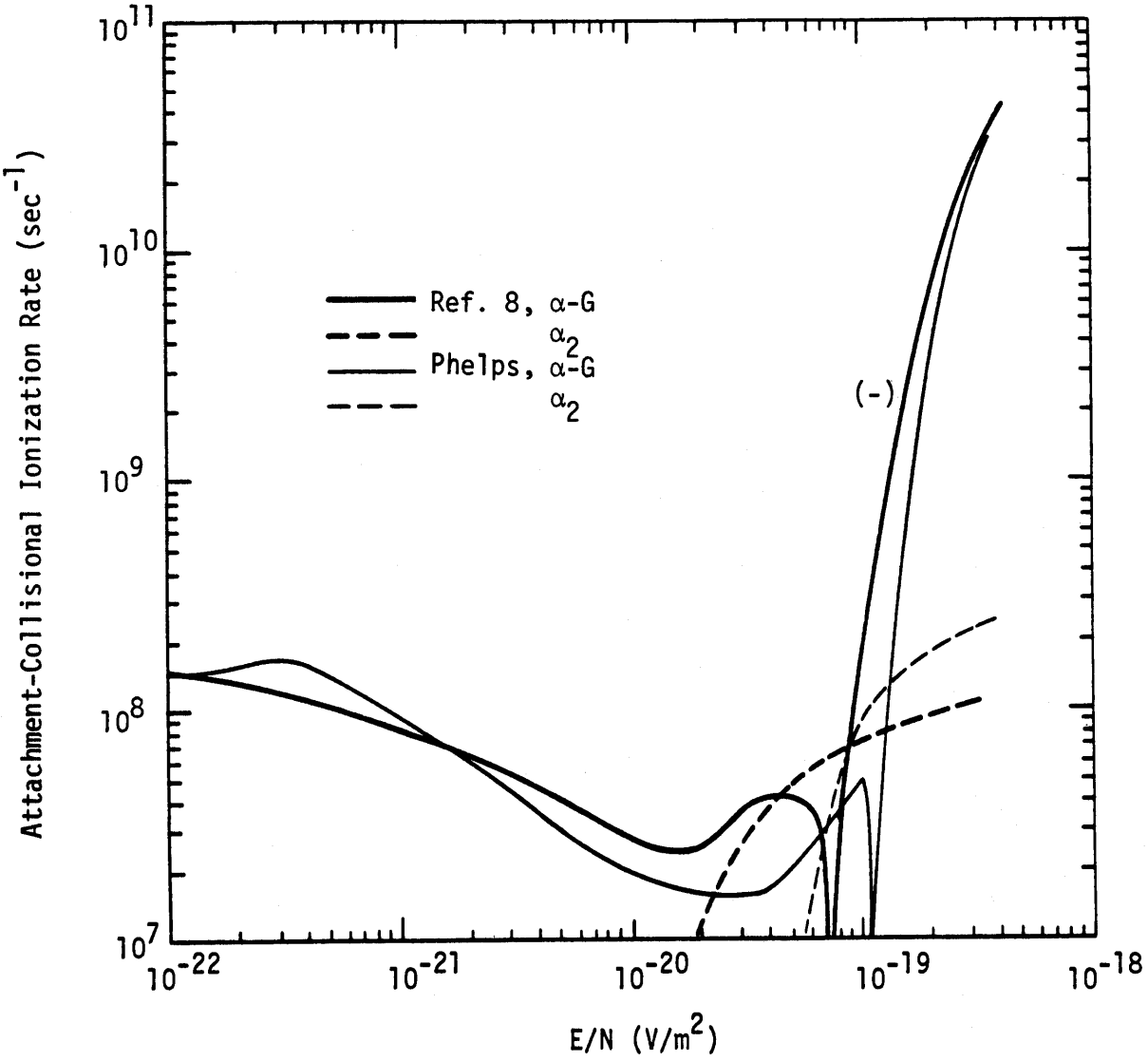

Figure 11. Two-body attachment rate and collisional ionization rate as reported by Phelps (Private Communication) and by Longley and Longmire (Ref. 6) compared.

e. Detachment (Reference 9)

Negative ions detach electrons, which allows for an additional source of electrons at high temperatures, primarily through collisions of negative ions with gas molecules.

$$D_{eo}(s^{-1}) = \frac{8.97 \times 10^{-19} (3.53 \times 10^{12} E/N)^{16.2}}{1 + 1.52 \times 10^{-23} (3.53 \times 10^{12} E/N)^{14.1}} \quad (59)$$

where E/N is in V-m^2.

3. THERMAL BEHAVIOR

a. Energy Input

Gallimberti (Ref. 10) has described the way energy from an electric field couples to a weakly ionized plasma. The electric field accelerates the electrons and dissipates power, $P=\vec{J}\cdot\vec{E}$ into kinetic energy of the electrons. That energy is transferred to the ions and neutral species by inelastic and elastic collisions. The energy deposited in the gas is initially partitioned into various forms of internal energy--translational, rotational, vibrational, electronic exciations, dissociation and ionization. Of these forms, all except the vibrational energy rapidly relax into a thermal equilibrium with each other. The vibrational states come into thermal equilibrium with the other forms of internal energy on a time scale which cannot be ignored in the calculation--we are therefore led to consider two temperatures for the gas. The first of these is the vibrational temperature determined by the equation of state of the vibrational states and the energy in the vibrational reservoir. The second is the "gas" temperature which is determined by a reduced equation of state (the vibrational degrees of freedom have been removed from the usual equation of state) and the "thermal" reservoir which contains all the energy in the gas except for that in the vibrational reservoir.

The flow of Joule heating energy through the system is shown in Figure 12. A fraction of f_V of this energy directly excites the vibrational states, and the remainder goes into the gas thermal reservoir. The calculations performed here use, for regions above the tip where Joule heating is important,

$$f_V = 0.56\ (1-f_D) \tag{60}$$

where f_D is the fraction of the gas molecules which are dissociated, as determined by the gas temperature. This fraction is consistent with the detailed calculations of Capitelli and Molinari (Ref. 11) who performed detailed rate calculations of each of the vibrational states in molecular hydrogen. Gallimberti (Ref. 10) used a value $f_V = 0.8$ in his calculations of natural lightning leaders in air.

Rate equations for the collisional decay of vibrational states into the thermal pool are given by Gallimberti (Ref. 10). These are:

$$\frac{dW_V}{dt} = f_V \vec{E} \cdot \vec{J} - \frac{W_V(T_V) - W_V(T_g)}{\tau_V}$$

and

$$S_a = f_T \vec{E} \cdot \vec{J} - \frac{W_V(T_V) - W_V(T_g)}{\tau_g} \tag{61}$$

where T_V is the vibrational temperature, T_g the gas temperature, $\vec{E}\cdot\vec{J}$ the Joule heating rate, S_a is the rate at which energy is added to the thermal pool, and τ_V is the vibrational state decay time. Finally, the equation of state used for the vibrational system is

$$W_V = \frac{N\varepsilon_V}{e^{\varepsilon_V/kT_g} - 1} \tag{62}$$

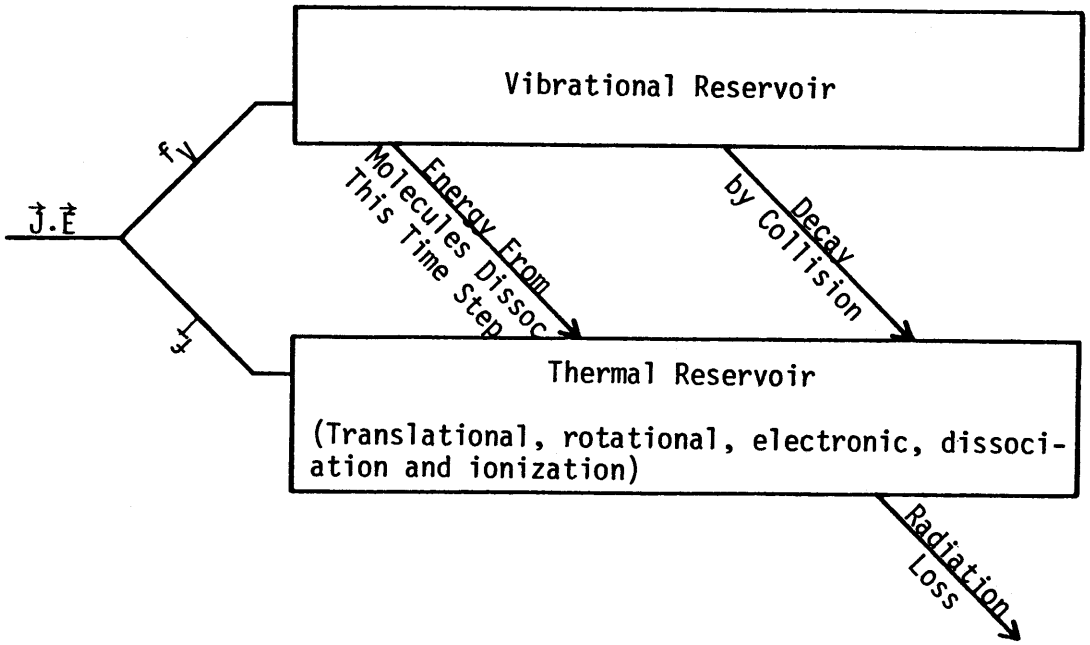

Figure 12. Flow of heat through system.

where ε_V = 0.27 eV is a weighted average of the separation of the vibrational levels of oxygen and nitrogen. The gas density is N and k is Boltzmann's constant. A curve fit to Gallimberti's (Ref. 10) results is used for the decay time τ_V. That curve fit is:

$$\tau_V = 6.779 \times 10^{-7} \, T_g^{-2.016} \tag{63}$$

where τ is in seconds and T_g is in units of electron volts (11600 K).

As the gas is heated molecules thermally dissociate and transfer their vibrational energy into the thermal reservoir. The thermal reservoir loses energy by radiation. The gas is assumed to be optically thin and the rate of loss of internal energy due to radiation is

$$\frac{\partial Q}{\partial t} = - \frac{8\pi^5 k^4}{15 h^3 c^2} \kappa_p \, T_g^4 \tag{64}$$

where Q is the gas internal energy, T_g the gas temperature, h Planck's constant, k Boltzmann's constant, c the speed of light, and κ_p is the Planckian mean opacity, and is assumed to be the curve fit (Ref. 13)

$$\kappa_p(T_g) = \frac{T_g^{5.14}}{1 + 0.0316 \, T_g^{5.64}} \tag{65}$$

At this point we have established the need for and considered the behavior of two energy reservoirs in addition to energy stored in the electrons, the thermal and vibrational reservoirs, and the dynamic interplay between them. Remaining is consideration of the cooling gas flow and the equations of state governing the various reservoirs.

b. Gas Flow

As the tip propagates forward into a new region in space it meets new, cooler air. This gas flow problem is properly handled in the gas and heat flow continuity equations by the convective derivative term. For the gas internal energy the continuity equation is

$$\frac{\partial Q}{\partial t} + \nabla \cdot (\vec{v}Q) = S_a \tag{66}$$

Since the flow of the gas (in the frame of the moving tip) is in the opposite direction to that of the motion of the tip, Equation 66 becomes

$$\frac{\partial Q}{\partial t} - v_z \frac{\partial Q}{\partial z} = S_a \tag{67}$$

where v_z is the tip velocity in the laboratory frame. This equation may be coupled into the remaining equations and solved by finite difference methods. However, the system evolves slowly. Since we are looking for a steady state solution, the differential equation may be integrated under steady state conditions (i.e., $\partial Q/\partial t$ assumed 0 in Equation 67) to derive an equilibrium internal energy. The steady state internal energy is used throughout for the gas temperature because its use greatly speeds convergence of the calculations. The steady state internal energy is given by

$$Q_{ss}(z') = \frac{1}{v_z} \int_{z\ \text{outer}}^{z'} S_a(z)dz \tag{68}$$

This form of accounting for gas flow is used for both the vibrational and thermal reservoirs.

c. Equations of State

There are now three temperatures to be considered, electron, vibrational, and gas. Once the appropriate internal energy is established the corresponding temperature is needed.

The electron velocity distribution is considered to be solely determined by the electric field. A curve fit to results of Baum (Ref. 12) is used.

$$T_e = 2.98 \times 10^{-3}(E)^{0.46} \tag{69}$$

where E is in V/m. This temperature is used when considering reactions which depend on collisions with electrons.

The equation of state for the vibrational states is given by Gallimberti (Ref. 10) and stated earlier in Equation 62. For the gas, the situation is more complex, since the contributions to the inernal energy due to dissociation and ionization must be considered. A reduced equation of state for a hot gas, (which has vibrational degrees of freedom removed) is described by Plooster (Ref. 15). For this equation of state populations of molecules, atoms, singly ionized, and doubly ionized species are calculated using the Saha equation. Dissociation and ionization energies are computed from weighted averages of the values for nitrogen and oxygen. For reference, the constants used are given in Table 2. The fraction of molecules which are dissociated, A_o, is

$$A_o = 2/[1 + (1+2B_o)^{1/2}]$$

where

$$B_o = C_o \rho T^{-1/2} \exp(I_o/RT) \tag{70}$$

The fraction of atoms which are once ionized, A_1, is

$$A_1 = 2/[1 + (1+2B_1)^{1/2}]$$

where

$$B_1 = C_1 \rho T^{-3/2} \exp(I_1/2RT) \tag{71}$$

TABLE 2. PHYSICAL CONSTANTS AND PARAMETERS USED IN COMPUTATIONS (AFTER PLOOSTER[15]).

Symbol	Specific second ionization	Value	Units
P	Gas constant	2.87096	J kg^{-1} K^{-1}
I_0	Specific dissociation energy	2.92013×10^7	J kg^{-1}
I_1	Specific first ionization energy	9.53764×10^7	J kg^{-1}
I_2	Specific second ionization energy	2.05472×10^8	J kg^{-1}
C_0	Constant in Saha equation for dissociation	0.331131	
C_1	Constant in Saha equation for first ionization	1.09763×10^7	
C_2	Constant in Saha equation for second ionization	2.06082×10^7	
T_o	Ambient temperature	300	K
P_o	Ambient pressure	1.01325×10^5	N m^{-2}
ρ_o	Ambient density	1.17681	kg m^{-3}

The fraction of singly ionized atoms which are doubly ionized is

$$A_2 = 2/[1 + B_2 + (1+6B_2+B_2^2)^{1/2}]$$

$$B_2 = C_2 \rho T^{-3/2} \exp(I_2/2RT) \qquad (72)$$

The internal energy of the gas is then computed from:

$$Q = \rho(RT[\tfrac{1}{2}(5+A_o) + 3(A_1+A_2)] + A_o I_o + A_1 I_1 + A_2 I_2) \qquad (73)$$

where

ρ is the gas density

$I_i (i=0,2)$ are the energies of dissociation or ionization

R is the gas constant

T is the gas temperature (Kelvins if the values in Table 1 are used).

It is assumed that the reactions take place serially, that is, all molecules are completely dissociated before ionization begins, all dissociated molecules are ionized once before second ionization begins. This technique allows two-species solution of each Saha equation rather than simultaneous solution of all species. Further, local thermodynamic equilibrium is assumed for calculation of the equation of state. Each of the A_i are calculated from the Saha equation and are therefore complex functions of temperature. Finding the temperature for a known internal energy density requires numerical solution of Equation 29. To minimize computation a table was generated and solutions to Equations 29 were found by linear interpolation of table values. Comparison of this equation of state for temperatures between 1200 and 12000 K with the perfect gas law and a commonly used curve fit (Ref. 14) are shown in Figure 13.

4. SOLUTION OF THE CONTINUITY EQUATIONS

Using the above set of equations for the rate constants, the equations of continuity may now be solved to calculate the populations of the three species of charged particles. Each species obeys a continuity equation assuming a constant growth velocity of the tip as did the thermal continuity equation and reflects the mobility in the electric field. The three continuity equations are where the radial convection has been neglected.

$$\frac{\partial n_e}{\partial t} - v_z \frac{\partial n_e}{\partial z} = S_\gamma + G n_e - a_{ei} n_e n_p + D_{eo} n_n - \alpha n_e \qquad (74)$$

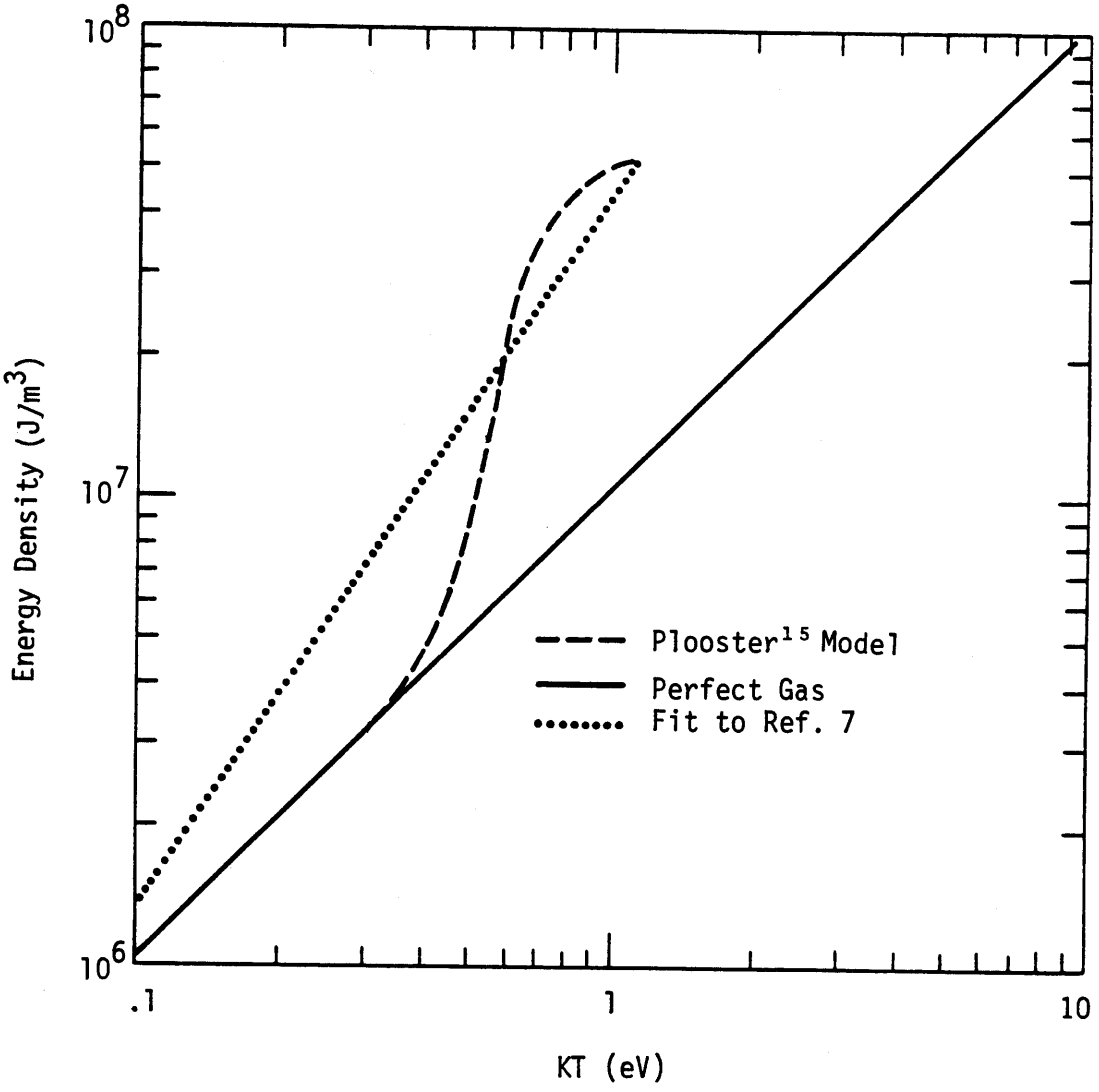

Figure 13. Comparison of various equations of state.

$$\frac{\partial n_p}{\partial t} - v_z \frac{\partial n_p}{\partial z} = S_\gamma + G n_e - a_{ii} n_n n_p - a_{ei} n_e n_p \tag{75}$$

$$\frac{\partial n_n}{\partial t} - v_z \frac{\partial n_n}{\partial z} = \gamma n_e - D_{eo} n_n - a_{ii} n_n n_p \tag{76}$$

where, n_e, n_p, and n_n are the respective electron, positive ion, and negative ion densities and the rate coefficients are as defined above. The source S_γ is the ion source from the background radiation. This source of electrons is negligible for the channel once established.

The geometry of the one-dimensional code is a narrow cone in spherical coordinates as shown in Figure 14. Spherical coordinates are necessary to insure the $1/r^2$ focusing of the current. It must be noted that the $1/r^2$ terms that would normally occur in the convective derivative do

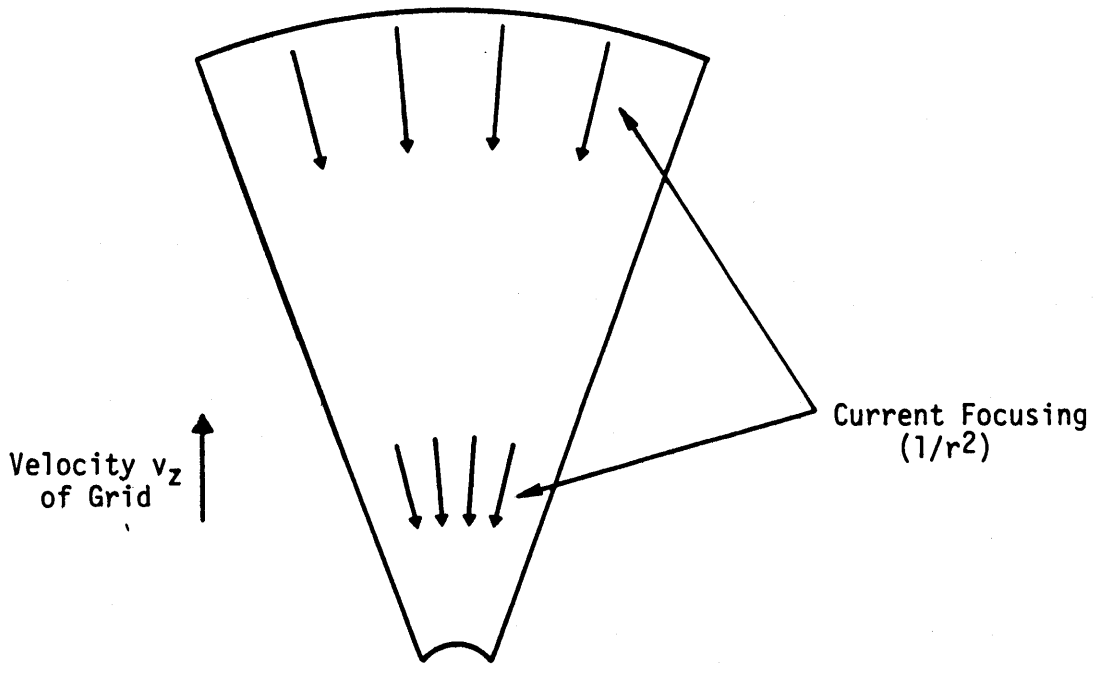

Figure 14. Geometry used in one-dimensional code.

not occur since the gas flow velocity field is uniformly z-directed and does not focus as does the current onto the tip of the lightning channel. These equations may be solved by explicit finite difference techniques.

a. Conductivity

The conductivity of the gas, which provides coupling between the electrical part of the problem and the air chemistry, is given by

$$\sigma_g = (n_e\mu_e + n_p\mu_p + n_n\mu_n)e \tag{77}$$

where μ_n and μ_p are the respective ionic mobilities, μ_e is the electronic mobility and e is the electronic charge. The mobilities of the heavy ions are relatively constant, much smaller than the electron mobility and are approximated by (Ref. 6)

$$\mu_n = 8 \times 10^{17}/N_g \quad m^2/V\text{-}s$$

and

$$\mu_p = 6.7 \times 10^{17}/N_g \quad m^2/V\text{-}s \tag{78}$$

Since the conductivity is more sensitive to the electronic mobility it is calculated by more precise means. Curve fits to data provided in a review paper by Dutton (Ref. 17) provided the following estimates for the drift velocity of the electrons, for resistivity due to collision with neutral atoms alone. The Dutton values have been augmented using the Landshoff-Spitzer plasma electrical conductivity relation to account for the added resistivity due to collisions of electrons with ions.

$$\frac{1}{\mu_e} = \frac{E}{v_{de}} = \frac{E}{3.73 \times 10^3 (E/N)^{0.707}} + 65.3\, n_e \ln\Lambda\, T_e^{-3/2}$$

for $E/N < 100$ Td

and

$$\frac{1}{\mu_e} = \frac{E}{v_{de}} = \frac{E}{1.63 \times 10^3 (E/N)^{0.913}} + 65.3\, n_e \ln\Lambda\, T_e^{-3/2} \tag{79}$$

for $E/N > 100$ Td

where E/N is in $T_d(10^{13}$ V-m$^2)$, v is in m/s and T_e is in units of 11600 K and

$$\Lambda = \frac{12\pi}{e^3}\left[\frac{\varepsilon_o^3 k^3 T_e^3}{n_e}\right]^{1/2} \tag{80}$$

k is the Boltzmann constant, T_e is the electron temperature, m_e is the electron mass and n_e is the electron density.

b. Linearized Calculation of n_e and E

Early in the study it became clear that stability of this coupled set of nonlinear differential equations was going to be a problem. The reason for this is that the electron density is a very sensitive function of the electric field--the avalanche and attachment rates are much larger than other rates involved in the calculations. To improve the stability at that point in the calculation an implicit linearized solution to the equations are inserted. In functional form Equation 74 may be written

$$\frac{\partial n_e}{\partial t} = f(n_e, E) \tag{81}$$

and since the electric field is a function of conductivity which is also a function of n_e and E, the electric field may be expressed as

$$E = g(n_e, E) \tag{82}$$

In the following, the new value of a quantity has superscript n and the corresponding previous time step (or old) values have superscript o. Differences between the two have a preceding Δ (e.g., Δn_e). Expanding Equations 81 and 82 in a first order Taylor series in n_e and E results in the following linearized equations in Δn_e and ΔE.

$$\Delta n_e = \Delta t\left(f^o + \Delta n_e \frac{\partial f}{\partial n} + \Delta E \frac{\partial f}{\partial E}\right) \tag{83}$$

and

$$\Delta E = \Delta E \frac{\partial g}{\partial E} + \Delta n \frac{\partial g}{\partial n} \tag{84}$$

These two equations are then solved simultaneously for the appropriate Δn_e and ΔE. It became necessary later, in some calculations, to limit ΔE and Δn_e to 20 percent of the old values, each time step.

c. Completed One-Dimensional Model

In the last few sections we have gathered those tools necessary to complete the determination of species populations and other quantities as a function of radius and time, as we approach the hot tip of the channel. As a review, the calculation of the environment proceeds as in the flowchart in Figure 15. Initial conditions are first specified with the avalanche field value for E and consistent values for the charged particle densities. The various temperatures are set to ambient values, since the code is somewhat insensitive to them on the first time step.

The simultaneous solution of the linearized equations for n_e and E is then performed, followed by calculation of the rate coefficients as functions of the newly calculated n_e and E as well as the thermodynamic variables. After the new rates are established the continuity equations for all three charged particle densities are advanced. It is important to solve for all three, including n_e, to maintain charge neutrality.

After the population of the various species is known along with their mobilities, the gas conductivity and the ohmic heating rate $\dot{Q}$ may be calculated.

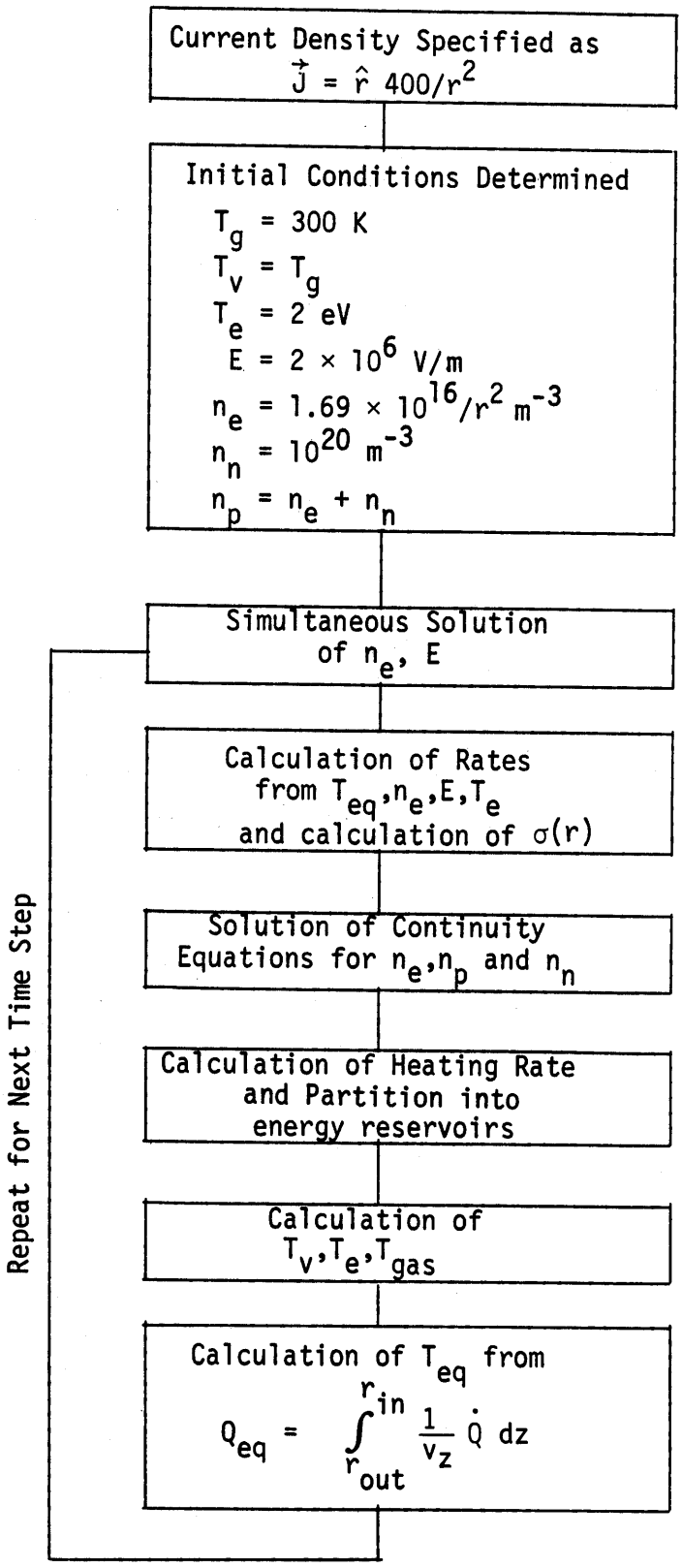

Figure 15. Flow chart of one-dimensional code.

$$\dot{Q} = \sigma E^2 \tag{85}$$

The energy input to the system is then partitioned into the vibrational and thermal reservoirs. The thermal reservoir is allowed to radiate as noted in the section on thermal behavior. Internal energy of the gas is converted to temperature via the equations of state. An equilibrium temperature is calculted using the new heating rate.

5. RESULTS OF ONE-DIMENSIONAL CALCULATIONS

Evolution of three important quantities to their equilibrium values as a function of radius are shown in Figures 16, 17 and 18. In Figure 16 the electron density is shown. Its variation from the original $1/r^2$ form is not large. Gas temperature is the slowest quantity to evolve and generally determines the total time to evolve to steady state. In Figure 18 the electric field evaluation is shown. An important feature is the maximum of the electric field near the tip. That maximum denotes the beginning of the tip region and is an indicator used in determination of the tip velocity.

For these one-dimensional calculations a value of $v = 10^5$ m/s has been assumed for the tip velocity. This value correspond to the observed value of the discharges on the MIKE shot (Ref. 1). For the value of the velocity the calculations reach a steady state value as noted in Figures 16, 17 and 18.

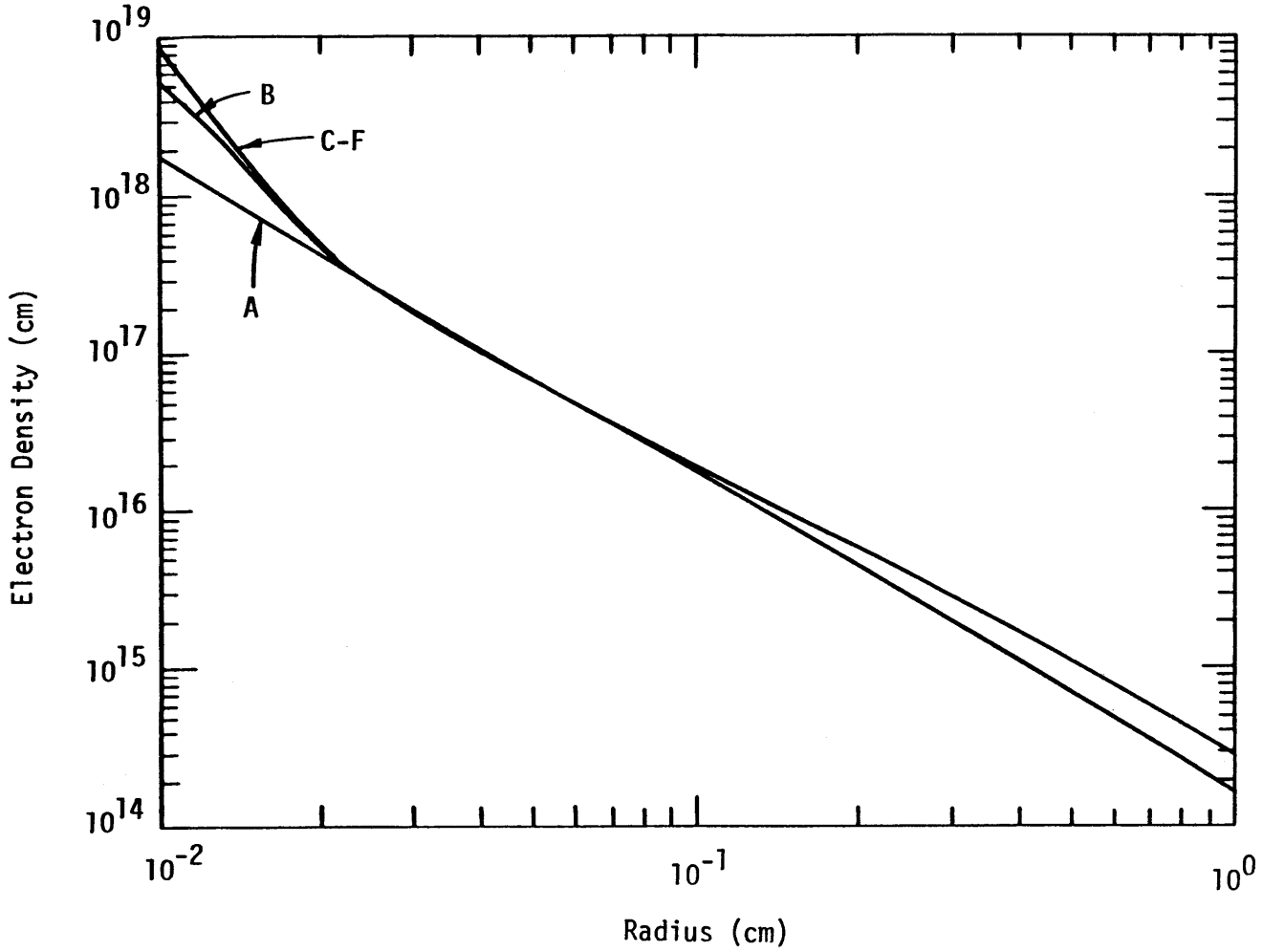

Figure 16. Time evolution of electron density as a function of radius. (Curve A is after one cycle, curves B through F represent later times. Time is nonuniform so no units are given.)

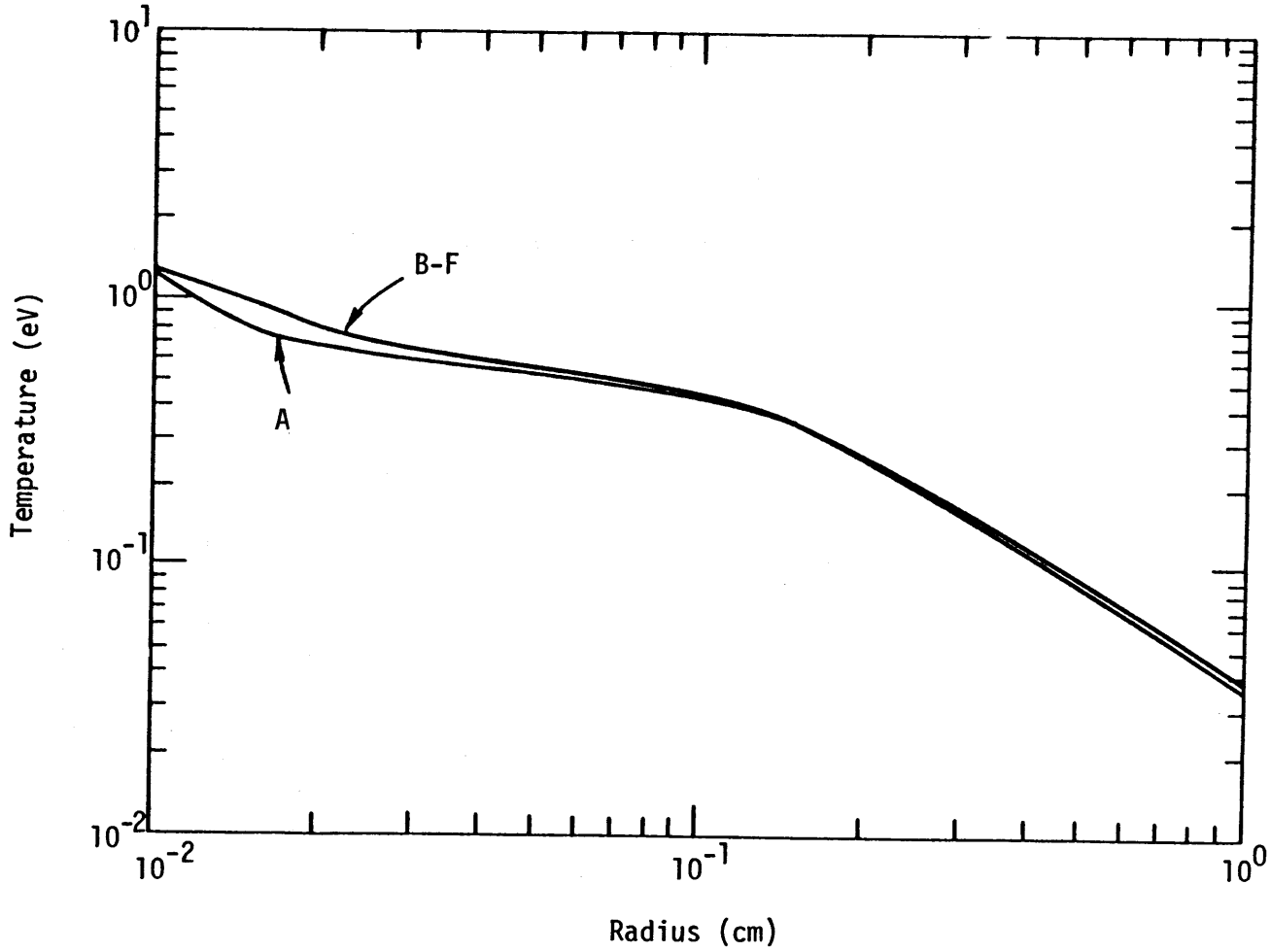

Figure 17. Time evolution of gas temperature (steady state calculation) as a function of radius. (Curve A is after one cycle, curves B through F represent later times. Time is nonuniform so no units are given.)

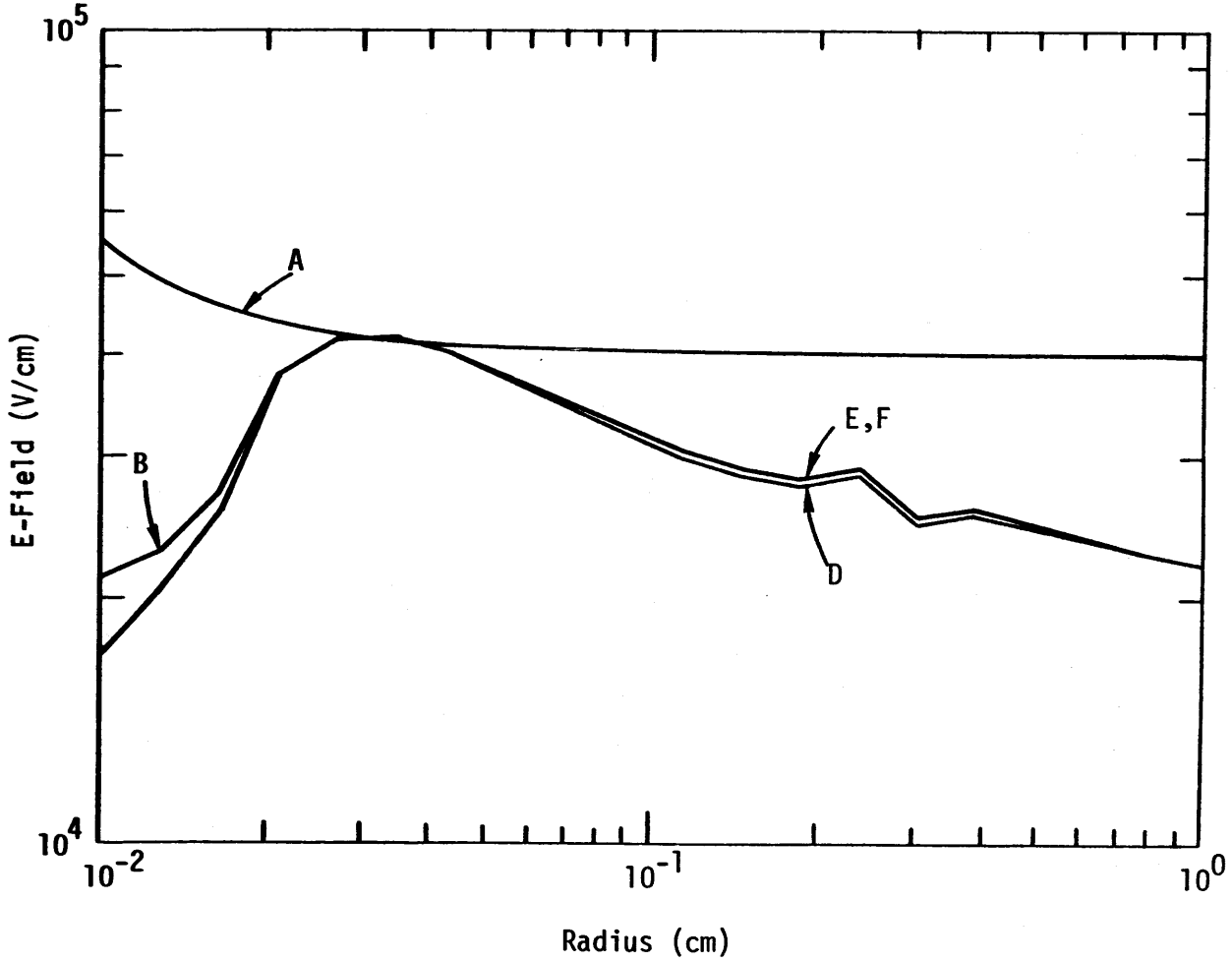

Figure 18. Electric field evolution as a function of radius. (Curve A is after one cycle, curves B through F represent later times. Time is nonuniform so no units are given.)

VII. TWO DIMENSIONAL CODE

After it was determined that the one-dimensional test bed was working properly and predicting the behavior close to the tip in a way consistent with the basic physics of the regime, the test bed was expanded to two dimensions and converted to prolate spheroidal coordinates. In addition, the current was determined by a solution to Poisson's equation so that the current could also adjust to the tip conditions. The prolate spheroidal coordinates used for the axially symmetric tip is shown in Figure 19. Zone sizes, as shown in the figure, were nonuniform and chosen to maintain maximum detail in the calculation near the hot tip.

1. SOLUTION TO POISSON'S EQUATION

Rather than specifying the current density as was done in the one-dimensional test bed, the current density is determined so that it obeys

$$\nabla \cdot \vec{J} = 0 \tag{86}$$

since there is no net sink or source of charge (i.e., $\partial\rho/\partial t = 0$). Applying Ohm's law and the definition of the static potential, ϕ, Equation 86 becomes

$$\nabla \cdot (\sigma \nabla \phi) = 0 \tag{87}$$

Except for the spatially dependent conductivity, this is just Poisson's equation and this equation and Equations 74 through 76 may be solved simultaneously using an iterative technique.

a. Solution Technique

Equation 74 may be expanded into prolate spheroidal coordinates (Ref. 18)

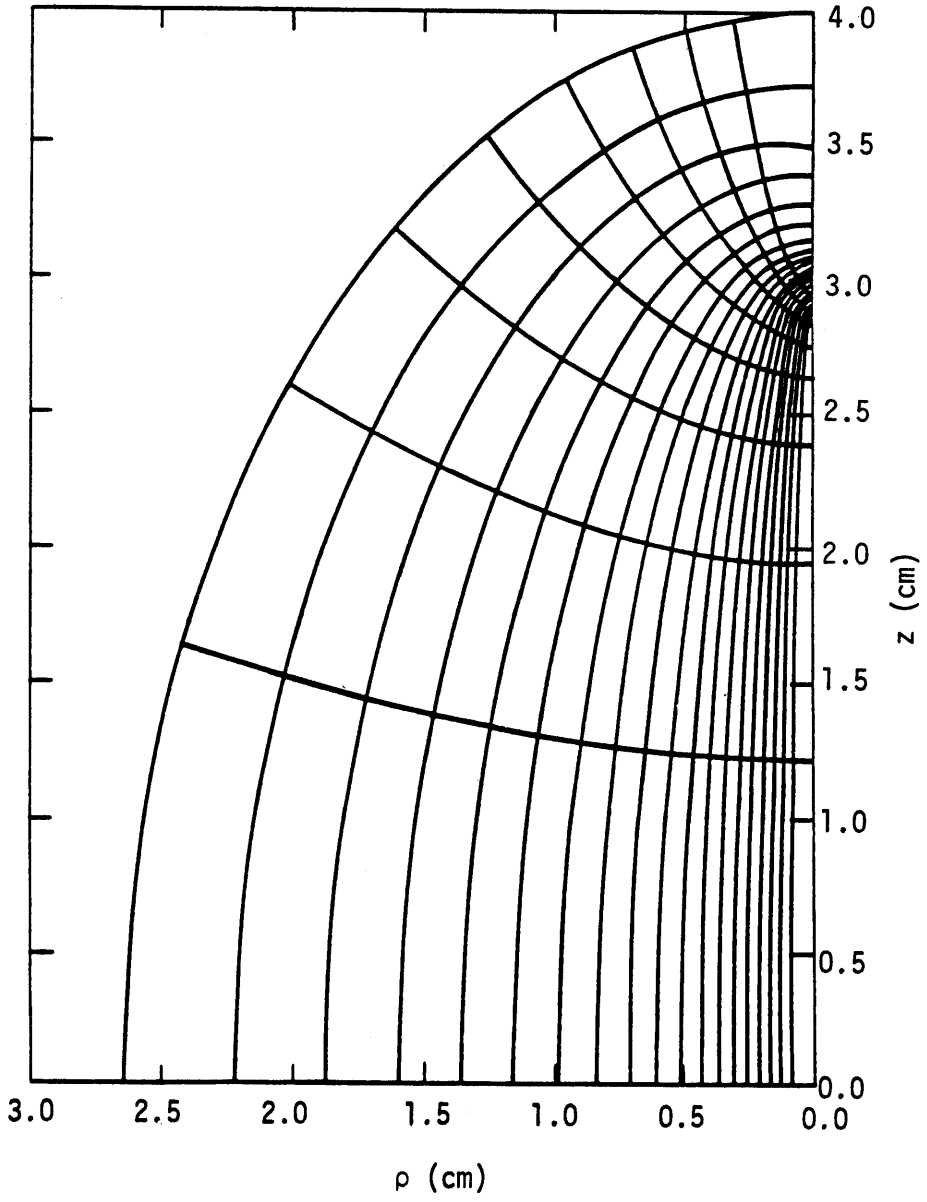

Figure 19. Tip geometry.

$$\frac{\partial}{\partial\xi}\,(\xi^2-1)\sigma(\xi,\eta)\,\frac{\partial\phi}{\partial\xi}+\frac{\partial}{\partial\eta}\,(1-\eta^2)\sigma(\xi,\eta)\,\frac{\partial\phi}{\partial\eta} \tag{88}$$

A mesh end is formed using coordinates ξ,η defined on an unequally spaced grid ξ_i, η_j. Within that grid a linearly centered set of difference equations is formed by differencing Equation 88, where the potential at coordinates ξ_i, η_j is expressed as

$$\phi(\xi_i,\eta_j) \equiv \phi_{ij} \tag{89}$$

$$\begin{aligned}
&\frac{1}{\xi_{i+1}-\xi_{i-1}}\left[2(\xi^2_{i+1/2}-1)\;\frac{\sigma_{i+1,j}+\sigma_{ij}}{2}\,\frac{(\phi_{i+1,j}-\phi_{ij})}{\xi_{i+1}-\xi_{i-1}}\right.\\
&\qquad\left.-\,2(\xi^2_{i-1/2}-1)\,\frac{\sigma_{i-1,j}+\sigma_{ij}}{2}\,\frac{(\phi_{ij}-\phi_{i-1,j})}{(\xi_i-\xi_{i-1})}\right]\\
&+\frac{1}{\eta_{j+1}-\eta_{j-1}}\left[2(1-\eta^2_{j+1/2})\,\frac{\sigma_{ij+1}+\sigma_{ij}}{2}\,\frac{\phi_{ij+1}-\phi_{ij}}{\eta_{j+1}-\eta_j}\right.\\
&\qquad\left.-\,2(1-\eta^2_{j-1/2})\,\frac{\sigma_{ij}+\sigma_{ij-1}}{2}\,\frac{\phi_{ij}-\phi_{ij-1}}{\eta_j-\eta_{j-1}}\right]=0
\end{aligned} \tag{90}$$

At the centerline bottom half, $\xi=1$ and, $i=I$ the limiting value at the centerline must be used.

$$\begin{aligned}
&-\frac{2}{\Delta\xi_I}\,\frac{\sigma_{Ij}+\sigma_{I-1,j}}{2}\,(\phi_{Ij}-\phi_{I-1,j})\\
&+\frac{1}{\eta_{j+1}-\eta_j}\left[2(1-\eta^2_{j+1/2})\,\frac{\sigma_{Ij+1}+\sigma_{iJ}}{2}\,\frac{\phi_{Ij+1}-\phi_{Ij}}{\eta_{j+1}-\eta_j}\right.\\
&\qquad\left.-\,2(1-\eta^2_{j-1/2})\,\frac{\sigma_{Ij}+\sigma_{Ij-1}}{2}\,\frac{\phi_{Ij}-\phi_{Ij-1}}{\eta_j-\eta_{j-1}}\right]=0
\end{aligned} \tag{91}$$

On the centerline top-half, $\eta=1$, $j=J$.

$$\frac{1}{\xi_{i+1} - \xi_{i-1}} \left[2(\xi^2_{i+1/2} - 1) \frac{\sigma_{i+1,J} + \sigma_{iJ}}{2} \frac{\phi_{i+1,J} - \phi_{iJ}}{\xi_{i+1} - \xi_i} \right.$$

$$- 2(\xi^2_{i-1/2}) \frac{\sigma_{iJ} + \sigma_{i-1J}}{2} \frac{\phi_{iJ} - \phi_{i-1J}}{\xi_i - \xi_{i-1}}$$

$$\left. + 2 \frac{\sigma_{iJ} + \sigma_{iJ-1}}{2\Delta\eta_J} (\phi_{iJ} - \phi_{J-1}) \right] = 0 \qquad (92)$$

And finally at the last point, $\xi=1$, $\eta=1$, which is the center of the grid or the tip of the channel.

$$\frac{(\sigma_{I-1,J} + \sigma_{IJ})(\phi_{IJ} - \phi_{I-1J})}{\Delta\xi_I} + \frac{(\sigma_{IJ} + \sigma_{IJ-1})(\phi_{IJ} - \phi_{IJ-1})}{\Delta\eta_J} = 0 \qquad (93)$$

For boundary conditions the potential is specified around the outside of the tip geometry and will be described in detail later.

The solution of the set of simultaneous linear equations is accomplished by the method of successive over-relaxation (Refs. 20 and 21). In this method the matrix representing the above difference equations may be solved by introducing a pseudo-time and allowing the system to relax to a static equilibrium. In matrix form the "time dependent" solution may be written

$$\frac{\partial \vec{\phi}}{\partial t} + \vec{\vec{A}} \cdot \vec{\phi} = \vec{g} \qquad (94)$$

The equation $\vec{\vec{A}} \cdot \vec{\phi} = \vec{g}$, may be reformed as

$$\vec{\vec{A}}' \cdot \vec{\phi} = \vec{g}' \qquad (95)$$

to that $\vec{\vec{A}}'$ may be written

$$\vec{\vec{A}}' = \vec{\vec{I}} + \vec{\vec{L}}' + \vec{\vec{U}}' \tag{96}$$

where $\vec{\vec{I}}$ is the unit matrix, $\vec{\vec{L}}'$ is a triangular matrix with zeros on and above the diagonal, and $\vec{\vec{U}}'$ is a triangular matrix with zeros on and below the diagonal. If a pseudo-time step (ω) is assumed in an explicit form of Equation 94 and a superscript p is used to denote the value of the quantity at the p^{th} time iteration then a method of solving Equation 94 is by iteration of the equation

$$\vec{\phi}^{p+1} = \vec{\phi}^{p} - \omega\vec{\vec{A}}'\vec{\phi}^{p} - \omega\vec{g}' \tag{97}$$

In Figure 20 the particular form of the equations approximating Poisson's equation on the mesh is evident. The potential at the central point is only dependent on the potentials at the four corners, i.e., at the north, N

$$\begin{array}{ccc} . & .N & . \\ .W & .C & .E \\ . & .S & . \end{array}$$

Figure 20. Local grid for Poisson's equation.

south, S, east, E, and west, W, points. For a particular sweep of the grid, two of the points S and W, say, have been determined by the time the equations for the central point C are solved. The updated points then form a better approximation to the potential at those points and so should be used. An improved equation then is

$$\vec{\phi}^{(p+)} = -\left[\vec{\vec{L}}'+\vec{\vec{I}}\right]^{-1}\vec{\vec{U}}'\vec{\phi}^{p} + \left[\vec{\vec{I}}+\vec{\vec{L}}'\right]^{-1}\vec{g}' \tag{98}$$

For $\omega \leq 1$, this is the Gauss-Seidel iteration procedure. For $\omega > 1$ it is known as the Successive Over-Relaxation method. For rectangular geometry, there is an optimum value for ω. However, for the prolate-spheroidal coordinates in this problem a value had to be determined by trial and error solution of a test problem for solution in the minimum number of iterations. The results were

$$\omega = 1 \quad \text{for 1st 7 iterations}$$

and

$$\omega = 1.55 \quad \text{thereafter.} \tag{99}$$

b. Boundary Conditions

As noted earlier, the potential on the boundary was forced to a particular solution consistent with the results of Reference 3. To form the boundary equations, Equations 90 were written in the form

$$\sigma_{ij} = g_{ij} \tag{100}$$

on the boundary. The values used are shown in Figure 21.

c. Current From the Potential

The current on the mesh was determined by:

$$\vec{J} = \sigma\vec{\nabla}\phi \tag{101}$$

and the total current found from the vector sum of the two orthogonal components. In the center of the mesh a centered differencing scheme is used with the value of the potential at the centralmesh point ignored. For the boundary values, the nearest two grid points to the boundary were used in noncentered form.

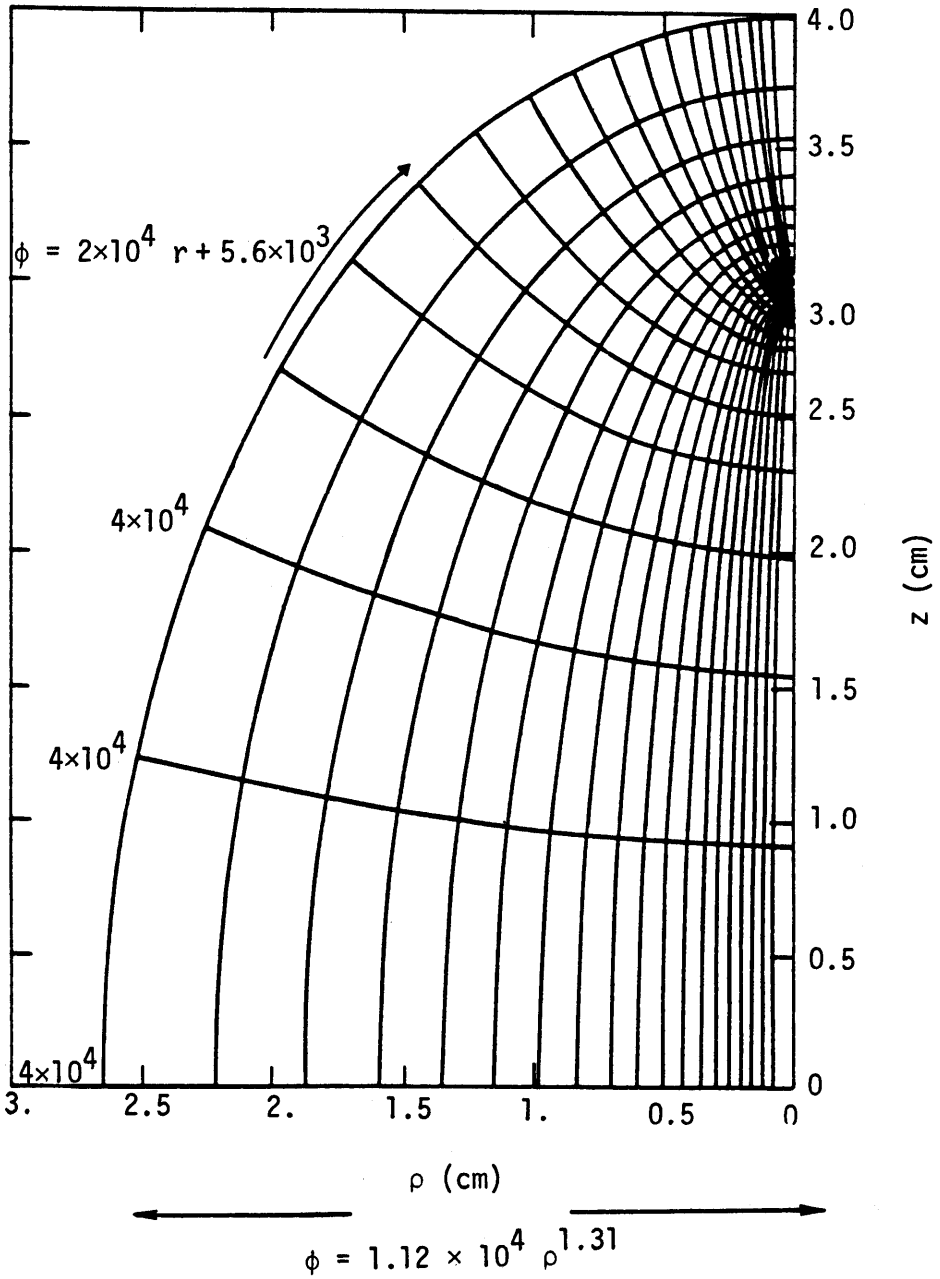

Figure 21. Potential on the boundary.

2. CONVERSION OF THE AIR CHEMISTRY EQUATIONS TO TWO-DIMENSIONS

After the current is determined from the solution to Poisson's equation the solution to the air chemistry problem near the tip proceeds in much the same way as for the one-dimensional case. Conversion to two-dimensions is aided by the fact that, with the exception of the convective derivatives in the continuity equations, all of the physical interactions are local. For example, the reaction rates at a given mesh point depend only on the electric field and temperature at that point.

The continuity equations vary from the one-dimensional case but are similar to each other. For electrons, Equation 74 in one-dimension becomes, since v is $-\hat{z}$ directed

$$\frac{\partial n_e}{\partial t} = \frac{2v_z}{a(\xi^2-\eta^2)} \left\{ \frac{\partial}{\partial \xi} (\xi^2-1)\eta n_e + \frac{\partial}{\partial \eta} [(1-\eta^2)\xi n_e] \right\}$$

$$= S_\gamma + G n_e - a_{ei} n_e n_p + D_{eo} n_n - \alpha n_e \qquad (102)$$

where a is a parameter in the coordinate system such that a/2 is the height of the tip. The remaining variables are as they are defined in the one-dimensional case. Continuity equations for n_p and n_n follow in the same form.

3. SOLUTION OF THE TWO-DIMENSIONAL EQUATIONS

All of the parts of the two-dimensional model have been described. All that remains is to review the way these parts fit together to model the behavior of the tip region. The flowchart in Figure 22 shows the sequence of calculation.

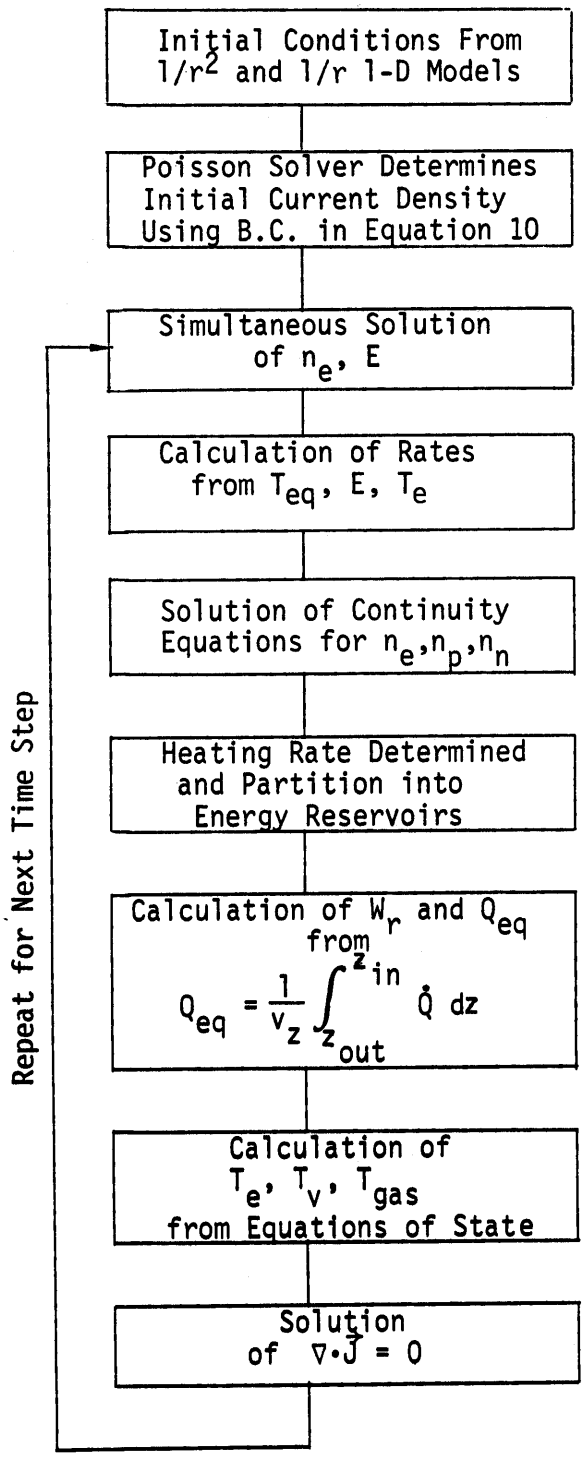

Figure 22. Flow chart of two-dimensional model.

Initial conditions are provided by separate application of solutions to the 1-D model using $1/r^2$ fixed current for the region ahead of the tip, $1/r$ fixed current along the sides, and a smooth variation between the two extremes. The conductivity from the 1-D models is then used as input to calculate the initial current density throughout the region of the tip. In the same way as in the 1-D solution, the local air chemistry near the tip for the 2-D model is determined from that current density. That is n_e and E are found simultaneously from the implicit solution described in the 1-D model. All rate coefficients are then found locally from T_{eq}, E, and T_e and inserted into the continuity equations. New particle densities for the three species result from solutions to the three appropriate continuity equations and are then used in the determination of a new conductivity profile. A new conductivity allows computation of the heating rate, less radiation losses, and therefore the internal energy in the vibrational, thermal, and electronic reservoirs. Calculation of the equilibrium internal energy is accomplished by the same z-path integrations as was used in the one-dimensional calculation. Various equations of state are used to calculate the temperatures associated with those internal energies. However, the line integration is made much more complex by the deviation of the constant coordinate lines in prolate spheroidal coordinates from a z = constant surface.

Finally, the conductivity profile is used to generate a new current density and the entire process is repeated. Time histories of all the thermodynamic variables, rates, and populations are then generated.

4. RESULTS OF 2D CODE

Although a run which was stable for indefinite run times was never achieved, that stability is very sensitive to the magnitude of the velocity of propagation of the tip. The most stable velocity was 1.2×10^5 m/s in agreement with the observed discharge seen on MIKE (Ref. 1).

Further, it was found that the two dimensional calculations lead to a tip which remains sharp, as observed, rather than expanding into a bulbous form and dissipating. The shape of the sharp temperature profile may be seen in the contour plot of temperature in Figure 23. The high thermal gradient is evident near the core. This thermal gradient leads to hydrodynamic expansion of the channel at some distance below the local diagram in Figure 23. Figure 24 is the analogous contour plot for electric field magnitude. The electric field reaches a maximum around 40 kV/m and rapidly goes to a very small field near the highly conducting core.

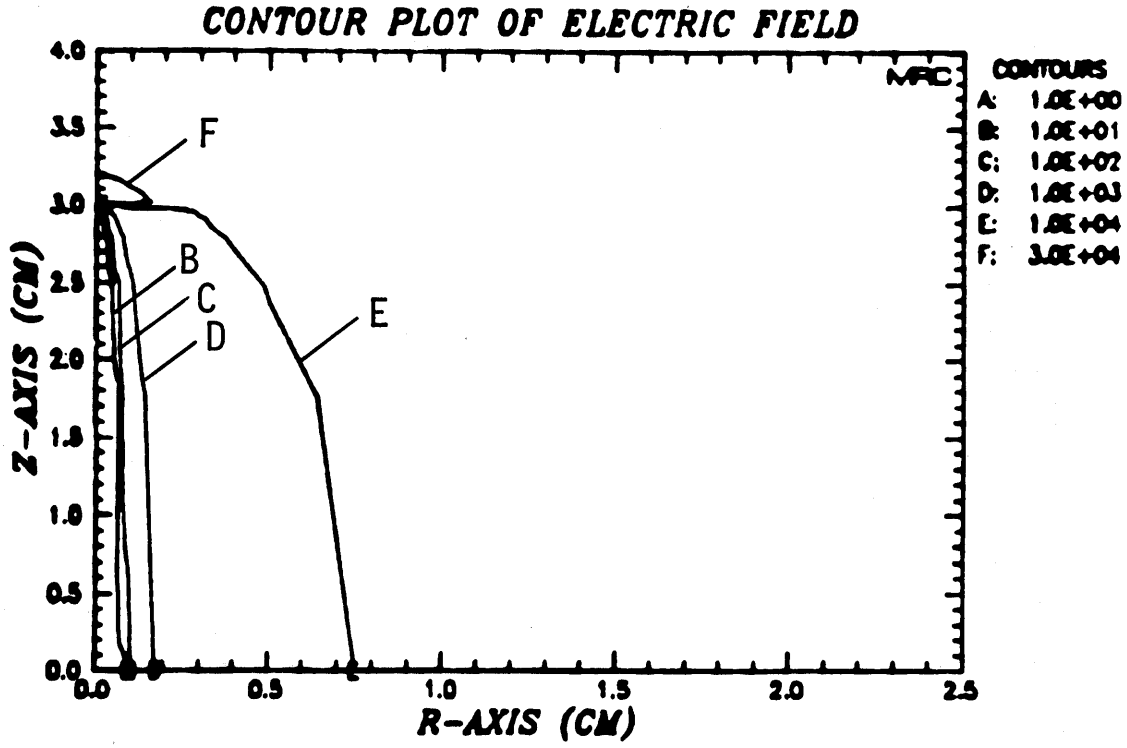

Figure 23. Contour plot of the interior field. The field in the highly conducting region near the tip is quite small. Contours are in units of 100 V/m.

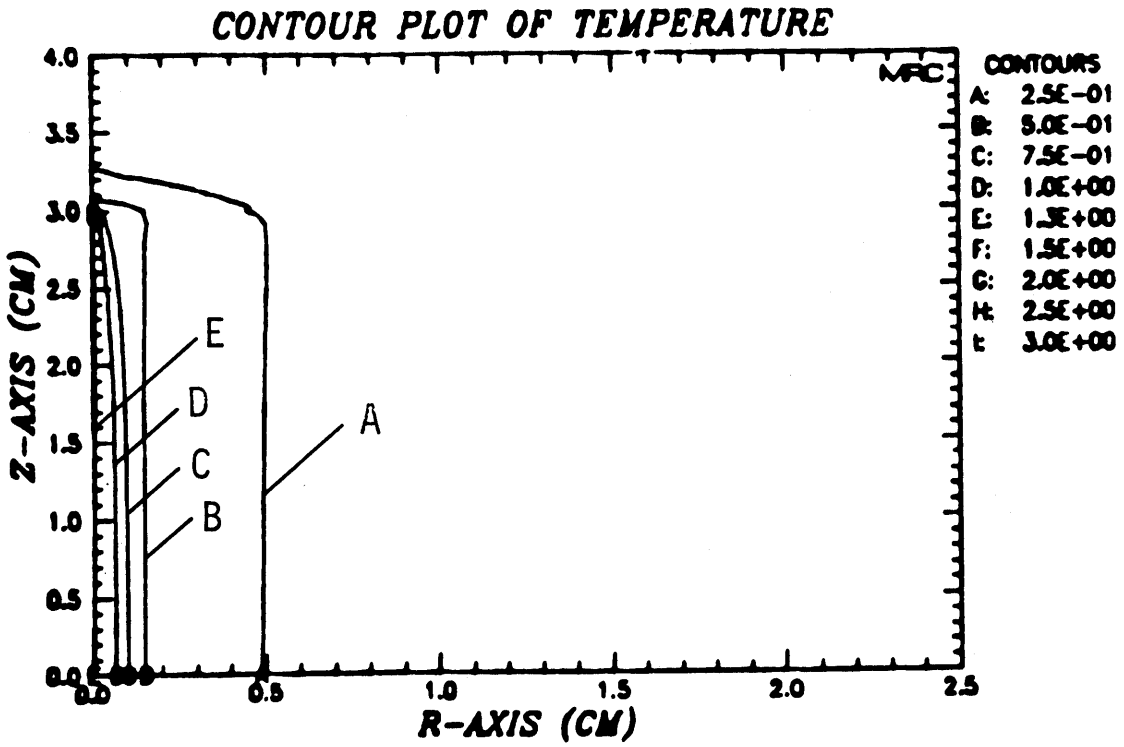

Figure 24. Contour plot of the gas temperature around the tip, showing the narrow tip formation. Contours are in units of 11600 K (1 ev).

VIII. CONCLUSIONS

The tip model discussed in this note represents a model of the characteristics of a nuclear lightning discharge. While this model is consistent with many of the observed details of nuclear lightning, natural lightning and laboratory sparks, many questions remain unanswered.

The air chemistry in the model is simplified and glosses over a number of important details of real air. For example, consideration of additional species in the air chemistry model would allow treatment of the different ionization, dissociation and attachment potentials of nitrogen and oxygen as well as species such as NO formed by atomic recombination. Chemical reactions in the air, particularly those involving vibrational states take time. Time dependent rate equations or complete solution of the master equations for the populations of the vibrational states should be accomplished to correctly treat dissociations.

The model presented here is steady state, while the actual nuclear lightning distance growth may well occur as a series of short bursts--the photographic evidence is not conclusive on this point. Some of the discharges observed split into several branches and there presently is no theory of this phenomena. If this bifurcation were extensive, it would lead to a substantial increase in the current at the base of a discharge. Further study of the stabiity of the solution for the discharge tip is extremely desirable.

A final subject in which further study would appear to be useful is the channel behind the tip. The model presented in this report assumes that the axial electric field within the discharge is much less than the ambient vertical electric field. The behavior of the channel behind the tip is determined by radiation transfer and hydrodynamic expansion which are rela-

tively unimiportant in the tip growth. The channel behavior is simplified, however, because the electron and ion densities should be in thermal equilibrium so that it would not be necessary to solve electronic rate equations. Based on experience with long sparks in air, the high currents are expected to produce a low channel resistance per unit length, but the simulation of channel behavior would yield a luminosity which could be correlated with photographic evidence.

In summary, the model presented here predicts a sharp, self-sustaining tip for the nuclear lightning discharges which propagates with the velocity observed photographically and provides the first quantitative solutions for the discharge currents.

REFERENCES

1. Uman, M. A., D. F. Seacord, G. H. Price, and E. T. Pierce, J. Geophys. Res., 77, (1977).

2. Longmire, C. L. IEEE Trans. on Ant. Prop., AD-26.

3. Longmire, C. L. and J. L. Gilbert, Theory of EMP Coupling in the Source Region, MRC-R-546, Mission Research Corporation, Santa Barbara, CA, January 1980.

4. Pitchford, L. C., S. V. O'Neil, and J. R. Rumkle, Jr., "Extended Boltzmann Analysis of Electron Sovanm Experiments," Phys. Rev. A, 23, No. 1, January 1981, p. 244-304.

5. Morgan, W. L., "ELENDIF" A Computer Program that Solves the Boltzmann Equation for a Partially Ionized Gas, JILA Information Center, Report No. 19, University of Colorado, Boulder, CO, 1 June 1979.

6. Marode, E., F. Bastien, and M. Bakker, "A Model of the Streamer Induced Spark Formation Based on Neutral Dynamics," J. Appl. Phys. 50 (1), January 1979, p. 140-146.

7. Gallimberti, I., "The Mechanism of the Long Spark Formation, "Journal de Physique, Colloque C7, Supplement in n 7, Tome 40, Juilht 1979, p. C7-123.

8. Longley, H. J. and C. L. Longmire, Electron Mobility and Attachment in Moist Air, MRC-N-222, Mission Research Corporation, Santa Barbara, CA, December 1975.

9. Goodson, D. W., R. O. Corbin, and L. Frommhold, "Electron Avalanches in Oxygen Detachment from the Diatonic Ion O_2^-," Phys. Rev. A, No. 5, May 1974, p. 2049-2059.

10. Gallimberti, I., "The Characteristics of the Leader Channel in Long Sparks," preprint.

11. Capitelli, M. and E. Molinari, "Kinetics of Dissociation Processes in Plasmas in the Low and Intermediate Pressure Range," Topics Curr. Chem. 90, 1980, p. 59-112.

12. Plooster, M. N., "Numerical Simulation of Spark Discharge in Air," Phys. FL. 14, No. 10, October 1971, p. 2111-2122.

13. Aids for Study of Electromagnetic Blackout, General Electric Company TEMPO, Handbook, DNA 3499K, p. 3-4, February 1975.

14. Baum, C. E., Electron Thermalization and Mobility in Air, AFWL Theoretical Note No. 12, Air Force Weapons Laboratory, Kirtland Air Force Base, NM, July 1965.

15. Plooster, M. N., Shock Waves from Line Sources, NCAR TN-37, National Center for Atmospheric Research, November 1968.

16. Aids for Study of Electromagnetic Blackout, General Electric Company TEMPO, Handbook DNA 3499H, p. 3-3, February 1975.

17. Dutton, J., "A Survey of Electron Swarm Data," J. Phys. Chem. Ref. Data, 4, No. 3, 1975, p. 577-856.

18. Morse, P. M. and H. Feshbach, Methods of Theoretical Physics, McGraw Hill Book Co., New York, 1953, p. 44, 1284.

19. Potter, D., Computational Physics, Wiley-Interscience, London, 1973, Ch. 4.

20. Ames, W. F., Numerical Methods for Partial Differential Equations, Academic Press, New York, Ch. 3, 1977.

APPENDIX A

POTENTIAL AND FIELD USED AS KERNEL IN POTENTIAL SOLVER

The potential at (r,z) due to the charge distribution shown in Figure A1 is a sum of the potential due to the four segments with linear charge density. Each of those has the form

$$\frac{1}{4\pi\varepsilon_o}\int_u^v \frac{(A\xi + B)d\xi}{\left(r^2 + (\xi-z)^2\right)^{\frac{1}{2}}}$$

$$= \frac{A}{4\pi\varepsilon_o}\int_u^v \frac{(\xi - z)d\xi}{\left(r^2 + (\xi-z)^2\right)^{\frac{1}{2}}} + \frac{(Az + B)}{4\pi\varepsilon_o}\int_u^v \frac{d\xi}{\left(r^2 + (\xi-z)^2\right)^{\frac{1}{2}}} \qquad \text{(A1)}$$

These integrals are straightforward

$$H_1(r,z,u,v) = \int_u^v \frac{d\xi}{\left(r^2 + (\xi-z)^2\right)^{\frac{1}{2}}} = \ell n\left[\frac{\left(r^2 + (v-z)^2\right)^{\frac{1}{2}} + v - z}{\left(r^2 + (u-z)^2\right)^{\frac{1}{2}} + u - z}\right] \qquad \text{(A2)}$$

$$H_2(r,z,u,v) = \int_u^v \frac{(\xi-z)d\xi}{\left(r^2 + (\xi-z)^2\right)^{\frac{1}{2}}} = \left(r^2 + (v-z)^2\right)^{\frac{1}{2}} - \left(r^2 + (u-z)^2\right)^{\frac{1}{2}} \qquad \text{(A3)}$$

Summing up the four contributions yields

$$\phi(r,z,a,b,c) = \frac{1}{4\pi\varepsilon_o}\left\{\frac{1}{b-a}\left[(z-a)H_1(r,z,a,b) + (z+a)H_1(r,z,-b,-a)\right.\right.$$

$$\left. + H_2(r,z,a,b) + H_2(r,z,-b,-a)\right]$$

$$- \frac{1}{c-b}\left[(z-c)H_1(r,z,b,c) + (z+c)H_1(r,z,-c,-b)\right.$$

$$\left.\left. + H_2(r,z,b,c) + H_2(r,z,-c,-b)\right]\right\} \qquad \text{(A4)}$$